A theoretical framework for microscopic surface and interface dipoles, work functions and valence band alignments in 2D and 3D halide perovskite heterostructures

Boubacar Traoré, Pooja Basera, Alexandra J Ramadan, Henry J Snaith, Claudine Katan, Jacky Even

A theoretical framework for microscopic surface and interface dipoles, work functions and valence band alignments in 2D and 3D halide perovskite heterostructures

Boubacar Traore,[*,†] Pooja Basera,[†,‡] Alexandra J. Ramadan,[¶] Henry J. Snaith,[¶] Claudine Katan,[†] and Jacky Even[*,‡]

†*Univ Rennes, ENSCR, CNRS, ISCR – UMR 6226, F-35000 Rennes, France*

‡*Univ Rennes, INSA Rennes, CNRS, Institut FOTON - UMR 6082, F-35000 Rennes, France*

¶*Clarendon Laboratory, Department of Physics, University of Oxford, Oxford, United Kingdom*

E-mail: boubacar.traore@univ-rennes1.fr; jacky.even@insa-rennes.fr

Abstract

We propose a computational methodology that highlights the intimate connection between surface and interface dipoles and work functions or valence band alignments. We apply the methodology to inspect the energy level alignments of halide perovskites and explore various situations relevant to perovskite-based heterostructures: i) the effect of surface termination, the ability to fine-tune and interpret the shift in energy alignments via ii) surface coating and iii) surface functionalization and / or passivation with molecules. We highlight the importance of local strain relaxation at the surfaces or interfaces, and revisit classical approaches based on capacitor models. Finally, we show that surface dipoles are additive in heterostructures and illustrate it through a 2D/3D perovskite interface. This provides a handy tool to interpret band alignments in complex perovskite-based heterostructures and buried interfaces. The scope of our work goes far beyond halide perovskites and can be useful to scrutinize the surfacial and interfacial behaviors of other semiconductors and heterojunctions. It allows bridging results from atomistic ab initio calculations and classical simulation approaches for multilayered thin film devices.

Introduction

Surfaces and interfaces are pervasive in thin films and semiconductor systems. They play a critical role in the performance of optoelectronic devices and the significance of their presence echoes well with the famous phrase "interface is the device".[1,2] This is because surfaces/interfaces offer additional flexibility to control the properties of devices through schemes such as: careful selection of contact materials, surface passivation and functionalization.[3,4] The latter, surface functionalization, directly influences the surface dipoles between adjacent layers in a device stack, which in turn change materials' work functions and absolute energy level alignments.[5–9] In the context of hybrid organic-inorganic halide perovskites (HOIP),[10–12] tuning the energy level alignment of materials composing the thin-film devices has been a successful strategy to improve their performance in photovoltaic cells and light emitting diodes (LEDs).[3,13–16] Indeed, a key ingredient to enhance the performance of optoelectronic devices is the appropriate energy level alignment between the photo-active layer and the contact charge carrier transport layers, namely the hole transport layer (HTL) and the electron transport layer (ETL).[17,18] An appropriate alignment allows the device to efficiently collect and transport the photo-generated carriers towards the electrodes for solar cells or improves the injection of carriers towards the photoactive layer for LEDs. Hence, a major playground for optimizing the performance of HOIP based devices is to fine-tune their energy level alignments and this may be achievable via surface functionalization and / or passivation.[3,19,20]

Although, the influence of surface passivation and / or functionalization on the change of work function is, in general, clear from experiments, the analyses rely on qualitative arguments or empirical models. This makes it difficult to quantify the effect of the change of surface dipoles on the change of work functions and absolute energy levels. To further elaborate on this missing link and bring a more quantitative analysis in the context of HOIP to be combined with results from existing experimental methodologies such as ultraviolet photoelectron spectroscopy (UPS) or inverse photoelectron spectroscopy (IPES) techniques,[2,21]

we revisit a methodology that clearly shows the relationship between surface dipoles and work functions.[22] The latter would correspond to absolute valence energy levels for undoped and non-defective materials of this family of semiconductors. We demonstrate the potentials of the methodology for hybrid semiconductors through a variety of cases to clearly show i) the effect of surface termination on the absolute energy level alignments, the ability to modulate the work function via ii) surface coating and iii) surface functionalization and / or passivation with molecules. Finally, we demonstrate the additivity of surface dipoles in heterostructures. The latter will be useful to design band alignments in complex heterojunctions and buried interfaces. Our methodology transcends the limits of halide perovskites and provides a computational strategy to fine-tune the absolute energy level alignments for optimizing the performance of broader families of optoelectronic devices.

Results and discussion

Link between the work function and the surface dipole

We start by establishing the expression that relates the work function to the surface dipoles using the International System of Units (SI). Beforehand, we present the steps that lead to the relation between the polarization density and the charge density. Using the definition of the displacement electric field:

$$\mathbf{D} = \epsilon_{\mathbf{0}}\mathbf{E} + \mathbf{P} \tag{1}$$

where $\mathbf{E}$ is the electric field and $\mathbf{P}$ is the polarization density that captures the field due to "*trapped*" dipole moments. Taking the divergence of Eq. (1) and comparing it to Gauss' law,

$$\epsilon_0 \nabla \cdot \mathbf{E} = \nabla \cdot \mathbf{D} - \nabla \cdot \mathbf{P} \tag{2}$$

and

$$\epsilon_0 \nabla \cdot \mathbf{E} = \rho \quad \text{with} \quad \rho = \rho_{free} + \rho_b \tag{3}$$

we have,

$$\begin{gathered} \rho = \nabla \cdot \mathbf{D} - \nabla \cdot \mathbf{P} = \rho_{free} + \rho_b \\ \text{with} \quad \nabla \cdot \mathbf{D} = \rho_{free} = 0 \quad \text{and} \quad -\nabla \cdot \mathbf{P} = \rho_b \end{gathered} \tag{4}$$

where ρ_{free} is the free charge density ($\rho_{free} = 0$ for dielectrics and insulators) and ρ_b is the bound charge density. Considering a slab with the vacuum along z (Figure 1a), one can consider the planar averaged charge density along z without loss of generality. Hence,

$$\rho_b(z) = -\frac{dP_z}{dz}. \tag{5}$$

From the integration by parts, the dipole moment density (surface dipole density) p is given by:

$$p = \int_{z_0}^{c/2} z\rho_b(z)dz = \int_{z_0}^{c/2} -\frac{dP_z}{dz} z dz = [-zP_z(z)]_{z_0}^{c/2} - \int_{z_0}^{c/2} -P_z(z)dz. \tag{6}$$

Assuming, by construction, that the dipole is vanishing in the middle of the bulk like layer of the slab ($z = z_0 = 0$, taken as the origin) and in the middle of the vacuum region (at $z = c/2$) (Figure 1a), the first term on the right hand side of Eq. (6) vanishes and we have the surface dipole p,

$$p = \int_{z_0}^{c/2} P_z(z)dz. \tag{7}$$

Eq. (7) can be numerically computed using the polarization density profile of Eq. (5), which is related to the total charge density $\rho_b(z)$, an output from first-principles calculations. Noteworthy, $\rho_b(z) = \rho_b(z)_{electronic} + \rho_b(z)_{ionic}$ is the total charge density including both electronic and ionic contributions. Notice that, at this stage, the procedure can be used to analyze only the microscopic contributions along the heterostructure stacking axis. This

semi-classical approach is analogous to the previous one used for dielectric susceptibility and microscopically induced dipole profiles.[23–25]

Inspired from the work of Leung *et al.*,[22] the last part of the theoretical development aims at relating the computed surface dipole p to the work function. As for the charge density, we consider the planar averaged potential $V(z)$ given by $V(z) = \frac{1}{A}\int\int dxdyV(x,y,z)$ where A is the area in the plane of the cell. Combining the definition of the dipole moment density (Eq. (6)) and Poisson's equation ($-\epsilon_0\nabla^2 V = \rho_b$):

$$p = \int_{z_0=0}^{c/2} z\rho_b(z)dz = \frac{-\epsilon_0}{A}\int dx \int dy \int_{z_0=0}^{c/2} z[\frac{\partial^2 V}{\partial x^2} + \frac{\partial^2 V}{\partial y^2} + \frac{\partial^2 V}{\partial z^2}]dz \tag{8}$$

Due to periodicity, the first two terms inside the bracket vanish. From the integration by parts of $\int_{z_0=0}^{c/2} z[\frac{\partial^2 V}{\partial z^2}]dz$, the terms $\frac{\partial V}{\partial z}$ at $z = z_0 = 0$ and $z = c/2$ disappear by the symmetry of the system. This results in

$$p = -\epsilon_0 \int_{z_0=0}^{c/2} dV(z) \Rightarrow \frac{p}{\epsilon_0} = V(c/2) - V(z_0) \tag{9}$$

If the Fermi level is set to zero (taken as the reference), then $-eV(c/2) = W_F = \phi$ is by definition the work function (Figure 1b). Therefore,

$$\begin{aligned} \phi &= -eV(z_0) - e\frac{p}{\epsilon_0} \\ \Rightarrow \Delta\phi &= e\frac{\Delta p}{\epsilon_0} = -1.809 \times 10^{-8}\Delta p \end{aligned} \tag{10}$$

where p is in C/m, ϕ in J, the charge e in C and ϵ_0 in F/m. Eq. (10) relates the change in the work function to the change of the surface dipole[22] and provides a consistent way to compare the results from energy level alignments. In other words, the change of the absolute valence energy alignments, due to a modulation and tuning of the surface properties, should be consistent with the numerically computed shift of the energy ($\Delta\phi$) as a result of the change of the surface dipoles. This will be shown in the subsequent studied systems.

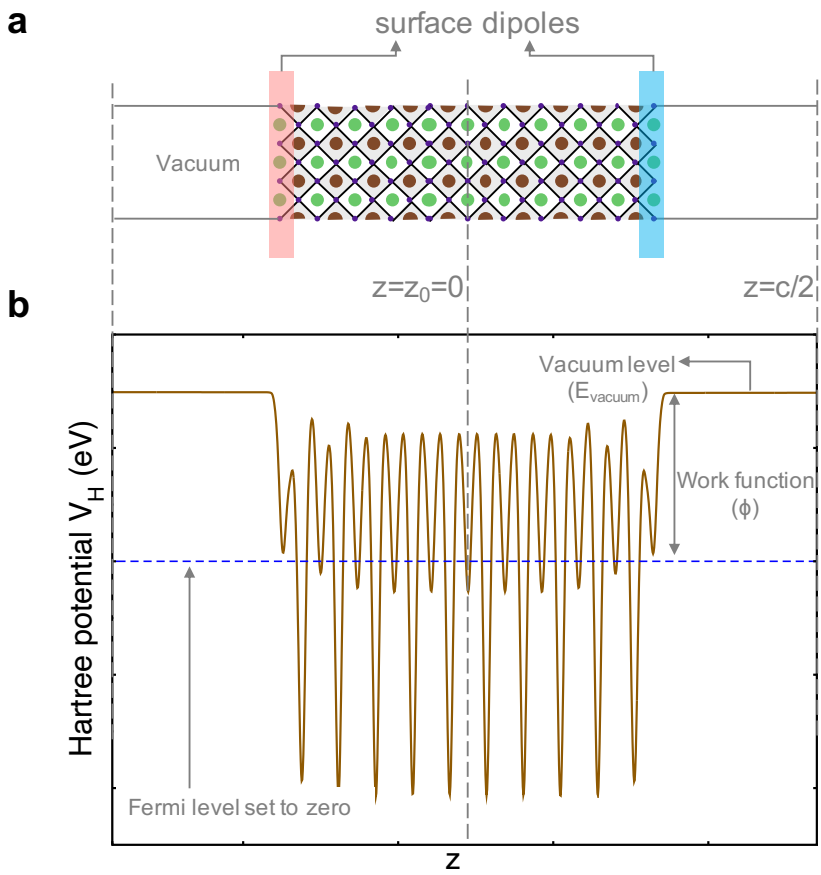

Figure 1: Definition of model parameters. **a** Slab structure used to define $z = z_0 = 0$ (center of the slab) and $z = c/2$ (middle of the vacuum) for the derivation of the surface dipoles. By construction, we use symmetrical terminations on either side of the surfaces such that the dipole moment is vanishing in the middle bulk like region at $z = z_0$. **b** Definition of the work function from a Hartree potential profile.

Effect of surface termination

We begin the application of the methodology considering two slabs : a $CsPbI_3$ slab from its pseudo-cubic structure[26] and low temperature orthorhombic $MAPbI_3$[27] slab (MA = methylammonium). We consider two different terminations hereafter named as CsI and PbI_2 for $CsPbI_3$ slab (Figure 2a) and MAI and PbI_2 for $MAPbI_3$ slab (Figure S1 and S2). With these two terminations, the most important features of the theoretical development from the previous section will be highlighted. Figure 2b presents an example of the shift of the Hartree potentials used to obtain the absolute valence energy alignments of the CsI structure shown in Figure 2a. Since, the atomic layers may reorganize differently when exposed to the vacuum

of the slab or attached to adsorbates, we also inspect the effect of surface layers relaxation on the surface dipoles and concomitantly on the absolute alignments. When the surface layers are unrelaxed in $CsPbI_3$ slab, we compute an absolute valence energy level (E_v^{abs}) of -6.78 eV for the PbI_2-terminated surface as compared to -4.51 eV for the CsI-terminated one as shown in Figure 2c. The difference amounts to $\Delta E_v^{abs} = 2.27$ eV between the two terminations. In the case of $MAPbI_3$, we obtain -5.30 eV and -6.92 eV for MAI and PbI_2 terminations, respectively (Figure 2g), resulting in $\Delta E_v^{abs} = 1.62$ eV. In both $CsPbI_3$ and $MAPbI_3$ slabs, PbI_2 termination presents a deeper E_v^{abs} as compared to the other termination when the surface layers remain unrelaxed.

To understand the microscopic origin of these large ΔE_v^{abs} differences, we compute the polarization density profiles of the two termination types using Eq. (5) as presented in Figure 2d,h. A few interesting features emerge from these profiles. Notably, the emergence of the surface dipoles which counteract each other at the opposite surface layers. Moreover, the surface dipoles fade away in the middle bulk-like region of the slabs justifying the assumption of vanishing dipole at $z = z_0$ in Eq. (7). We see from the areas under the peaks of the dipolar density profiles in Figure 2d,h that the PbI_2-terminated surfaces have larger surface dipoles as compared to the CsI and MAI-terminated ones. By integrating these profiles using Eq. 7, we calculate the difference of the surface dipole densities for the two terminations as summarized in Table 1. Notably, the differences of the absolute alignments ΔE_v^{abs} are in excellent agreement with the differences computed using Eq. (10). This shows that the increase of E_v^{abs} (ϕ) for PbI_2-termination is solely due to the increase of its surface dipole as compared to CsI or MAI-termination. The agreement between the Hartree potential alignment approach with theoretical prediction from Eq. (10), not only serves as a double check for consistent results but also underscores the link between surface dipoles and energy level alignments.

At the surface of a crystalline solid, the termination of the crystal structure and the absence of the subsequent ions/atoms, implies that the lowest energy relative position of the

surface atoms will be different as compared to the atoms within the infinite crystalline slab. We can allow the surface to "relax" computationally, and then estimate this impact upon the surface dipole for the different surface terminations. Hence, we compute the surface dipoles and E_v^{abs} of the different terminations for the relaxed surface layers of both slabs (Figure 2e,f for $CsPbI_3$ and Figure 2i,j for $MAPbI_3$) and the results are summarized in Table 1. Again, there is an excellent agreement between ΔE_v^{abs} and $\Delta\phi$ obtained from Δp. In the case of $MAPbI_3$, surface relaxation sligthly pushes E_v^{abs} down for both MAI and PbI_2 terminations with a minor effect on the sign and value of ΔE_v^{abs}. However, contrary to the unrelaxed case, E_v^{abs} for CsI-termination is larger than that of PbI_2-termination in $CsPbI_3$ slab. We obtain similar results for $CsPbBr_3$ slabs as discussed in the Supplementary Information (SI) (see Text S4 of the SI for the related discussion). This trend between the relaxed and unrelaxed surface layers can be anticipated from the lower surface dipole of PbI_2 as a result of surface relaxation. The changes are due to the combined effect of the octahedral distortions of the surface layer along with the contraction or the stretching of PbI bond lengths at the surface (see Text S5). This shows that in these ionic semiconductors, surface relaxation impacts the surface dipoles, which in turn directly tunes the subsequent absolute energy alignments and the work functions. It also highlights the importance of experimental techniques giving access to the local atomistic details at the surfaces and interfaces to probe the relaxation of the perovskite lattice. Finally, we shall point out that the differences between the work-functions obtained here for the relaxed and unrelaxed bare surfaces, may appear at first sight quite large. But in most pratical cases, such surfaces are, in addition, likely to be covered intentionnaly or naturally by passivation layers (*vide infra*).

Table 1: Comparison of absolute valence energy levels (E_v^{abs}) calculated for the different systems. The table also compares the shifts of absolute valence energy levels obtained from the difference of surface dipoles ($\Delta\phi$ using Eq 10) and those computed from the Hatree potential alignment (Figure 2b and Eq. 14). CsI or MAI-termination is taken as the reference when comparing to PbI_2. With the adsorbate X at the termination Y (X_Y, *e.g.* $DMSO_{CsI}$), the termination Y is used as the reference.

Unrelaxed surface layers				
	$E_v^{abs} = \phi$ (eV)	ΔE_v^{abs} (eV)	Δp (C/m)	$\Delta\phi$ (eV) [Eq. 1)]
		$CsPbI_3$ slab		
CsI	-4.51	-	-	-
PbI_2	-6.78	-2.27	$+2.01\times10^{-11}$	-2.27
		$MAPbI_3$ slab		
MAI	-5.30	-	-	-
PbI_2	-6.92	-1.62	1.44×10^{-11}	-1.63

Relaxed surface layers				
		$CsPbI_3$ slab		
CsI	-6.42	-	-	-
PbI_2	-5.73	$+0.69$	-0.62×10^{-11}	$+0.70$
Cs-coating$_{CsI}$	-3.54	$+2.88$	-2.54×10^{-11}	$+2.87$
Cs-coating$_{PbI_2}$	-3.10	$+2.63$	-2.33×10^{-11}	$+2.63$
$DMSO_{CsI}$	-4.66	$+1.76$	-1.54×10^{-11}	$+1.74$
$DMSO_{PbI_2}$	-4.53	$+1.20$	-1.05×10^{-11}	$+1.19$
$TMPPA_{CsI}$	-5.20	$+1.22$	-1.05×10^{-11}	$+1.19$
$TMPPA_{PbI_2}$	-5.74	-0.01	$+0.04\times10^{-11}$	-0.05
		$MAPbI_3$ slab		
MAI	-5.73	-	-	-
PbI_2	-7.36	-1.63	1.45×10^{-11}	-1.64
$DMSO_{MAI}$	-4.90	$+0.83$	-0.72×10^{-11}	$+0.81$
$DMSO_{PbI_2}$	-4.83	$+2.53$	-2.25×10^{-11}	$+2.54$
$TMPPA_{MAI}$	-5.09	$+0.64$	-0.55×10^{-11}	$+0.62$
$TMPPA_{PbI_2}$	-5.76	$+1.60$	-1.40×10^{-11}	$+1.58$

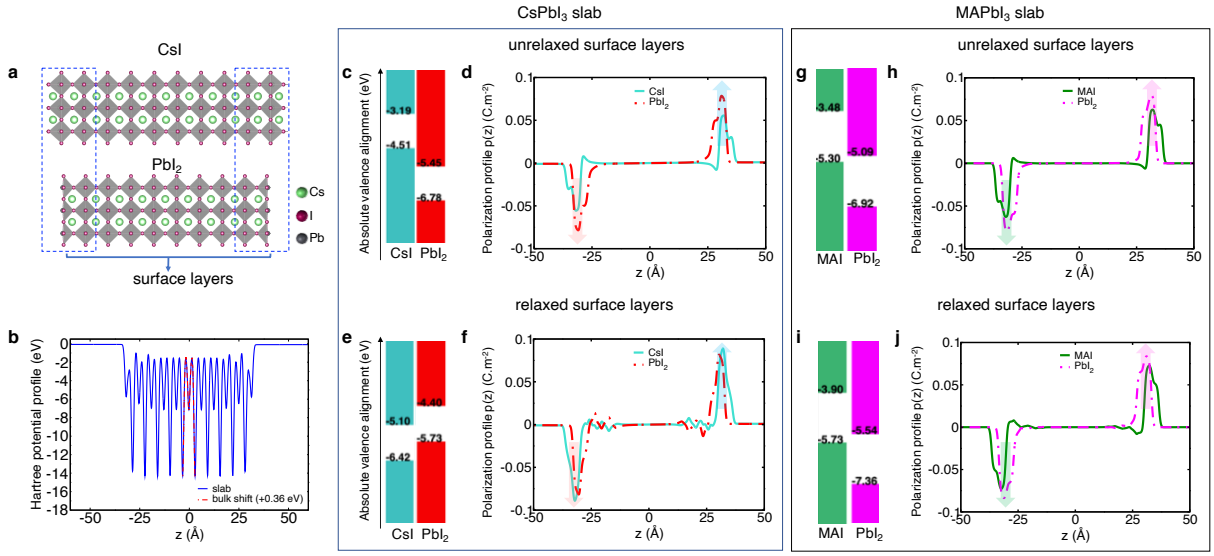

Figure 2: Effect of surface termination on absolute energy alignments and microscopic interpretation. **a** $CsPbI_3$ structures with CsI and PbI_2 terminations with relaxed surface layers. The surface layers are shown by dashed rectangles on either side of the slab. **b** Hartree potential alignment method used to obtain the absolute valence energy levels of the systems. The profile of the slab corresponds to the relaxed CsI terminated surface shown in **a**. For this example, a potential shift (ΔV_H) of +0.36 eV between the slab and the bulk results in superimposed profiles at the center of the slab (bulk-like region). **c** Computed absolute valence energy levels for CsI and PbI_2 terminated surfaces, respectively, for the unrelaxed surface of $CsPbI_3$ slab. **d** Polarization density profiles of the two terminations of $CsPbI_3$ slab showing different surface dipoles for the unrelaxed surface layers. The integration of these profiles result in the surface dipole moments of Eq. (7) discussed in the text. **e** Computed absolute valence energy levels of CsI and PbI_2 terminated surfaces, respectively, for the relaxed surface layers of $CsPbI_3$ slab. **f** Polarization density profiles of the two terminations of $CsPbI_3$ slab showing different surface dipoles for the relaxed surface layers. **g** Computed absolute valence energy levels of MAI and PbI_2 terminated surfaces, respectively, for the unrelaxed surface layers of $MAPbI_3$ slab. **h** Polarization density profiles of the two terminations of $MAPbI_3$ slab showing different surface dipoles for the unrelaxed surface layers. **i** Computed absolute valence energy levels for MAI and PbI_2 terminated surfaces, respectively, for the relaxed surface layers of $MAPbI_3$ slab. **j** Polarization density profiles of the two terminations of $MAPbI_3$ slab showing different surface dipoles for relaxed surface layers. The arrows pointing the directions of the dipoles are guides to the eyes.

Effect of the surface coating with Cs

Coating perovskite surfaces with a metal like Cs presents potential technological promises in applications requiring electron sources such as electron beam accelerator facilites.[28] It has recently been demonstrated that by depositing monolayers of Cs on top of halide perovskites, the electron emission efficiency was improved[29] and the improvement was attributed to a change of sign of the electron affinity, which translates into a diminishing work function.

Work function shifts obtained by DFT techniques can be compared to dedicated phenomenological models,[30] but we show here that the atomistic origin can be directly analyzed within the general theoretical framework proposed in the present work. To shed more light on this effect, we placed a monolayer of Cs (each monolayer contains 2 Cs atoms for 2 terminal I atoms) on top of either side of the relaxed surface layers of both CsI and PbI_2-terminated $CsPbI_3$ slabs. The insertion of Cs monolayer, hereafter referred to as Cs-coating, creates surface states at the bottom of the conduction band with the Fermi level crossing those bands, making the system n-type (Figure S6, Text S6). Concomitantly, the Fermi level becomes closer to the vacuum level. The computed E_v^{abs} values for Cs-coating are compared to those from the pristine CsI and PbI_2-terminated slabs in Figure 3 and Table 1. With Cs-coating, E_v^{abs} is reduced by about 2.88 eV as compared to the pristine CsI-terminated slab and 2.63 eV in the case of PbI_2-termination. This decrease of E_v^{abs} is further illustrated with the computationally reduced surface dipoles as a result of the surface coating with Cs (Figure 3c,f and Table 1). This reduction of the surface dipole is associated with the charge transfer from the Cs monolayer to the surface perovskite atoms as shown in Figure 3d,g. We observe charge depletion from the Cs monolayer which gets transferred to the perovskite layer. This induces a dipole pointing out from the surface and leads to the reduction of the absolute valence energy level or the work function. These results are consistent with the lowering of the onset energy of the electron emission by about 2.2 eV for $CsPbI_3$ due to the deposition of Cs monolayers from photoelectric experiments.[29] This difference is in fair agreement with 2.63 eV − 2.88 eV predicted from our calculations. Note that the shifts ΔE_v^{abs} with Cs-coating are in excellent agreement with $\Delta\phi$ computed via Eq. (10) as shown in Table 1.

Effect of the surface passivation and / or functionalization

Surface passivation and/or functionalization is a topic of considerable interest nowadays for developments of perovskite based thin film technologies. We refer the reader to the extensive

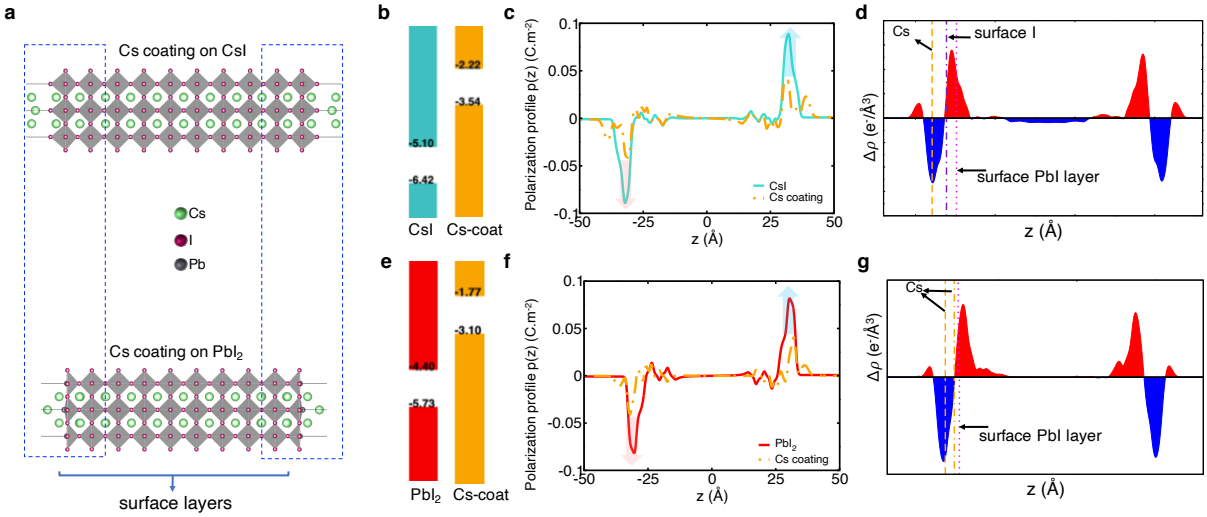

Figure 3: Effect of surface coating with Cs. **a** Comparison of relaxed $CsPbI_3$ structures with CsI and PbI_2 terminations with the surface layers coated with a monolayer of Cs. The surface layers are shown by dashed rectangles on either side of the slab. **b** Computed absolute valence energy levels of the slabs with CsI and a monolayer of Cs on CsI terminations. **c** Polarization density profiles comparing the surface dipoles of the slabs with CsI and a monolayer of Cs on CsI terminations. **d** Profile of the electronic charge density transfer across the slab with a monolayer of Cs on CsI-terminated surface. Red for electronic charge accumulation and blue for electronic charge depletion. The positions of Cs monolayer, surface I and PbI layers are shown by vertical lines. coated with a monolayer of Cs. The surface layers are shown by dashed rectangles on either side of the slab. **e** Computed absolute valence energy levels of the slabs with PbI_2 and a monolayer of Cs on PbI_2 terminations. **f** Polarization density profiles comparing the surface dipoles of the slabs with PbI_2 and a monolayer of Cs on PbI_2 terminations. **g** Profile of the electronic charge density transfer across the slab with a monolayer of Cs on PbI_2-terminated surface. Red for electronic charge accumulation and blue for electronic charge depletion. The positions of Cs monolayer and PbI layers are shown by vertical lines.

literature and reviews on these aspects,[2,31–38] but we want to illustrate via two examples how our proposed theoretical framework could suitably guide the ongoing experimental efforts. We choose as a first example the tuning of the surface dipoles by passivating and / or functionalizing $CsPbI_3$ and $MAPbI_3$ surface layers with DMSO (Dimethyl sulfoxide; Figure 4a), a commonly used solvent in halide perovskites fabrication process.[39,40] We consider both CsI and PbI_2-terminated surfaces for $CsPbI_3$ slab and MAI and PbI_2-terminated surfaces for $MAPbI_3$ slab. To insert DMSO at the surface, we place the oxygen (O) atom of the molecule at the position of an outer terminal I (iodine) atom.[41] In doing so, we remove a neighboring Cs atom or MA molecule to keep the charge neutrality of the system. In these

slabs, the pristine surfaces contains 2 outer I atoms and we substitute one of them by DMSO. Hence, we have a ratio of one DMSO molecule per 2 outer I atoms. The relaxation of the surface with DMSO induces octahedral distortions of the surface PbI layers (see Figure S7, S8 for the relaxed systems). For instance, the in-plane Pb-I-Pb angles of the relaxed $CsPbI_3$ surface layers with DMSO on the CsI-termination vary between $\sim 141°$ and $\sim 164°$ from the ideal undistorted 180°. These octahedral distortions cause a widening of the band gap in the surface region as can be seen from the layer-by-layer resolved projected density of states (PDOS) of the system in Figure S9. Nevertheless, the resulting band structure exhibits dispersive bands with no surface states inside the gap showing the passivating role of DMSO (Figure S10, S11). In all cases, the energy level alignment with DMSO at the surface pushes up the absolute valence energy levels of the different systems (Figure 4b-e). The corresponding polarization density profiles clearly indicate a severe reduction of the surface dipole with the addition of DMSO (Figure 4b-e and Table 1). Again, we find that the differences ΔE_v^{abs} in all the different terminations are in excellent agreement with $\Delta\phi$ computed via Eq. (10). The lowering of E_v^{abs} with DMSO is due to the reduction of the surface dipole as a result of charge transfer from DMSO to the outer perovskite layer (see for instance, Figure S12 for DMSO on the CsI-terminated surface). Considering the polarization profiles of Figure 4b and by integrating them, we obtain surface dipoles of about 2.52×10^{-11} C/m ($\sim$ 6.0 D) and 4.06×10^{-11} C/m ($\sim$ 9.7 D) for the slabs with DMSO and CsI termination, respectively. Hence, the resulting difference of $\sim 1.54 \times 10^{-11}$ C/m ($\sim$ 3.7 D) represents the contribution of DMSO to the total surface dipole. In the isolated slabs with DMSO molecules on the different terminations, we obtain a surface dipole of $\sim 2.7 - 2.9$ D in fair agreement with the experimental value of 3.9 D.[42] The calculated dipole moment for the isolated DMSO molecule is slightly lower than that obtained from the difference of the profiles of Figure 4b-e. We note that in the perovskite slab with DMSO, outer I and Cs ($CsPbI_3$ slab) or I and MA ($MAPb_3$ slab) were removed, which partly explain this difference in addition to the contributions coming from the interactions of the molecule with the perovskite surface.

Unlike purely classical methods (*vide infra*), this semi-classical approach provides a microscopic description of the role of surface dipoles in the shift of the surface potential barriers affecting work functions or absolute valence energy levels. The case study demonstrates a strategy to fine tune the energy level alignment of optoelectronic devices by a careful selection of the molecular compounds which could not only serve as passivating agents but also act as design parameters for adjusting the energy levels for more performing devices.

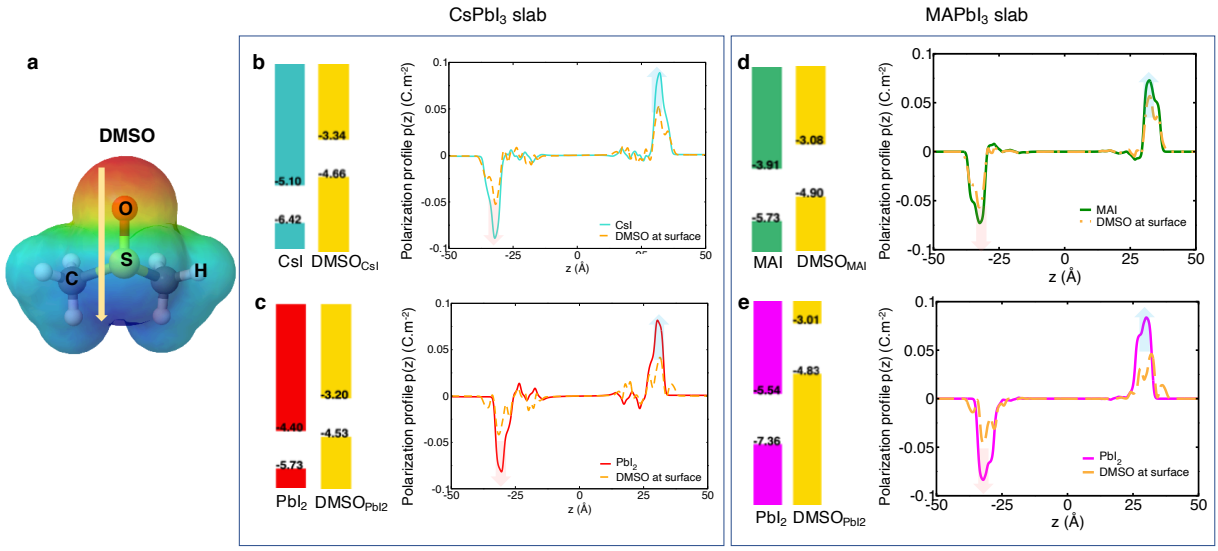

Figure 4: Effect of surface passivation and / or functionalization with DMSO. **a** DMSO molecule with the Hirshfeld net atomic charge map. Red for excess electronic charge and blue for electron deficiency. The arrow shows the direction of the dipole moment of DMSO, which points from O to S. **b** (left) Computed absolute valence energy levels of $CsPbI_3$ slabs with CsI and DMSO on CsI terminations. (right) Polarization density profiles comparing the surface dipoles of the slabs with CsI and DMSO on CsI terminations. **c** (left) Computed absolute valence energy levels of $CsPbI_3$ slabs with PbI_2 and DMSO on PbI_2 terminations. (right) Polarization density profiles comparing the surface dipoles of the slabs with PbI_2 and DMSO on PbI_2 terminations. **d** (left) Computed absolute valence energy levels of $MAPbI_3$ slabs with MAI and DMSO on MAI terminations. (right) Polarization density profiles comparing the surface dipoles of the slabs with MAI and DMSO on MAI terminations. **e** (left) Computed absolute valence energy levels of $MAPbI_3$ slabs with PbI_2 and DMSO on PbI_2 terminations. (right) Polarization density profiles comparing the surface dipoles of the slabs with PbI_2 and DMSO on PbI_2 terminations.

Finally, we consider (2,4, 6-trimethylphenyl)phosphonic acid (TMPPA) to passivate the surfaces of both $CsPbI_3$ and $MAPbI_3$ slabs. We use a similar approach as in DMSO to insert TMPPA at the surface. The relaxed structures with TMPPA at the surfaces are shown in Figure S13-S14 and the resulting band structures exhibit dispersive bands with no surface

states inside the gap showing the passivating role of TMPPA (Figure S15, S16). In all cases, the presence of TMPPA at the surface pushes up the absolute valence energy levels of the different systems (Figure 5b-e) except for TMPPA at PbI_2-termination in $CsPbI_3$ slab. The corresponding polarization density profiles clearly indicate a severe reduction of the surface dipole with the addition of DMSO (Figure 4b-e and Table 1). With TMPPA at PbI_2-termination in $CsPbI_3$ slab, the change in surface dipole is less significant ($\sim 0.04 \times 10^{-11}$ C/m, Table 1), which explains its similar E_v^{abs} as compared to $CsPbI_3$ with PbI_2-termination. Notably, the differences ΔE_v^{abs} for all the different terminations are in excellent agreement with $\Delta\phi$ computed via Eq. (10).

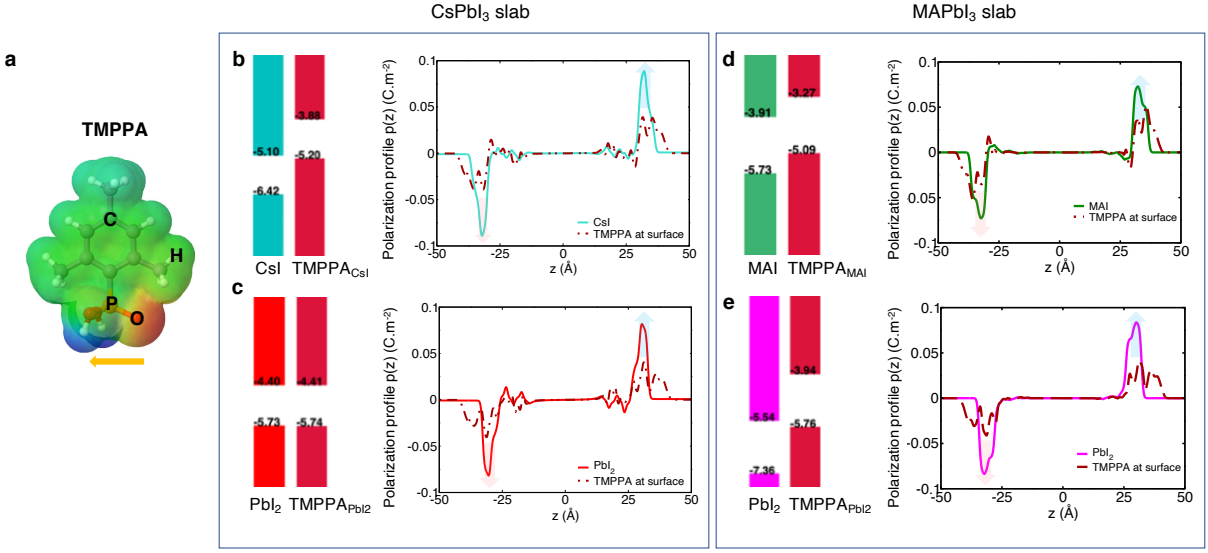

Figure 5: Effect of surface passivation and / or functionalization with TMPPA. **a** TMPPA molecule with the Hirshfeld net atomic charge map. Red for excess electronic charge and blue for electron deficiency. The arrow shows the direction of the dipole moment of TMPPA. **b** (left) Computed absolute valence energy levels of $CsPbI_3$ slabs with CsI and TMPPA on CsI terminations. (right) Polarization density profiles comparing the surface dipoles of the slabs with CsI and TMPPA on CsI terminations. **c** (left) Computed absolute valence energy levels of $CsPbI_3$ slabs with PbI_2 and TMPPA on PbI_2 terminations. (right) Polarization density profiles comparing the surface dipoles of the slabs with PbI_2 and TMPPA on PbI_2 terminations. **d** (left) Computed absolute valence energy levels of $MAPbI_3$ slabs with MAI and TMPPA on MAI terminations. (right) Polarization density profiles comparing the surface dipoles of the slabs with MAI and TMPPA on MAI terminations. **e** (left) Computed absolute valence energy levels of $MAPbI_3$ slabs with PbI_2 and TMPPA on PbI_2 terminations. (right) Polarization density profiles comparing the surface dipoles of the slabs with PbI_2 and TMPPA on PbI_2 terminations.

Additivity of surface dipoles and buried interfaces for a 2D/3D perovskite heterostructure

The different systems, thus far investigated, exhibit the clear connection between the surface dipoles and the tuning of energy level alignments. This occurs through the interaction between the dipoles of the different materials composing the whole structure. A natural question that could arise would be: How are the surface dipoles of the constituent materials connected to that of the combined structure viewed as a single entity? The analysis of complex heterostructures with buried interfaces is indeed important for practical applications. We address this issue by considering a heterostructure comprised of $CsPbI_3$ interfaced with BA_2PbI_4 (BA = Butylammonium) 2D perovskite. The details of the heterostructure construction and relaxation are provided in the SI. Here, the heterostructure is conceptualized as a multilayer nanocomposite[23,25] whereby it is divided into its components as shown in Figure 6a. We compare the polarization density profiles of the different structures in Figure 6b. We notice that at the interface region, the polarization profile of the 3D ($p(z)_{3D}$) counteracts that of the 2D ($p(z)_{2D}$) as a result of the opposing orientations of BA in the 2D and 3D-like regions, where the $[NH_3]^+$ groups of the molecule point to the perovskite. Notably, by adding the profiles $p(z)_{3D}$ and $p(z)_{2D}$, we recover the polarization profile of the heterostructure following:

$$p(z)_{heterostructure} \approx p(z)_{3D} + p(z)_{2D} \tag{11}$$

Eq. (11) provides a theoretical guidance for the engineering of complex 2D/3D heterostructures. It demonstrates the quasi-additivity of the surface dipoles across the heterostructure down to the atomic scale. Moreover, it highlights the interplay between the dipoles of the different systems that lead to the readjustment of the energy level alignments in interface systems as compared to the energy levels obtained in individual materials. This additivity of the surface dipoles in heterostructures is analogous to the additivity of the dielectric sus-

ceptibilities that was demonstrated in a previous work.[25] Together, they provide a variety of analysis methods to gain deeper insights on the optoelectronic properties of complex material heterostructures. We find similar results with $PEA_2PbI_4/CsPbI_3$ 2D/3D heterostructure (Figure S17) showing the generality of the approach (PEA=phenylethylammonium). Hence, this method can be very useful to interpret band alignments in complex heterostructures and buried interfaces.

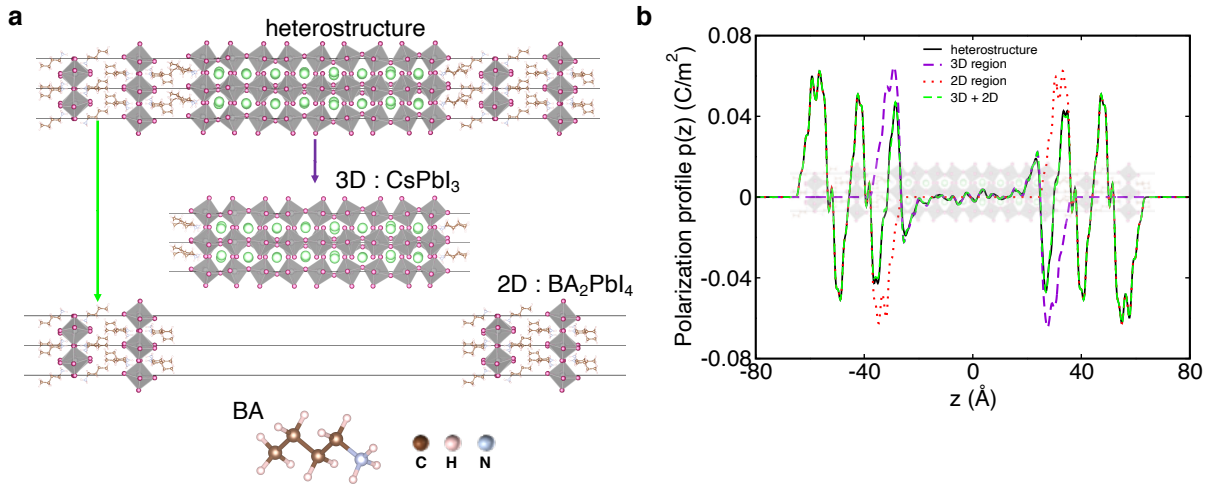

Figure 6: Additivity of the surface dipoles. **a** The relaxed 2D/3D heterostructure model composed of $CsPbI_3$ interfaced with BA_2PbI_4. The heterostructure is viewed as a composite showing its constituent parts. **b** Computed polarization density profiles of the 2D/3D and the constituent parts demonstrating the additivity of the surface dipoles down to the atomic scale.

Revisiting the classical approach to surface molecular dipoles

Following the pioneering work of Demchak and Fort,[43] an attractive model was developed to analyse monolayers at water-air interfaces, but later on applied more widely to describe ultrathin layers made of dipolar molecules separating two dielectric media. This model was adapted to various situations,[43–46] including the design of organic solar cells and optoelectronic devices.[47–50] This model also called the "three-Capacitor Model"[44,51] for the analysis of monolayers at water-air interfaces, provides a link between the potential drop across the stack ΔV, and three electric dipoles attributed to water molecules and the Langmuir monolayers:

$$\epsilon_0 A \Delta V = \frac{\mu_1}{\epsilon_1} + \frac{\mu_2}{\epsilon_2} + \frac{\mu_3}{\epsilon_3} \tag{12}$$

where A is the surface area and the three pairs of dipole moments and relative dielectric constants μ_i,ϵ_i $(i = 1, 2, 3)$ are respectively attributed to the aqueous subphase, polar head and hydrophobic tail end-groups of the adsorbed molecules. It must be pointed out that the deviation of the dipole moments with respect to the surface normal along the stack direction was also considered.[43,44] When used in the context of thin film based devices,[47,48,50] a similar formula is expressed in a more compact form, considering only the potential drop across the ultrathin dipolar molecular layer:

$$\Delta V = \frac{N.\mu.cos\theta}{\epsilon_0 \epsilon_r} \tag{13}$$

where N is the surface dipole density and θ is the angle between the molecular dipole (μ) and the normal to the surface. This formula provides a practical way to qualitatively describe the influence of molecular dipoles on device properties, but an adhoc choice of an effective dielectric permittivity ϵ_r has to be made in order to get a quantitative match between experimental quantities and computed potential drops. It should be noted that the problem of the arbitrary choice of effective dielectric permittivities was already documented in the literature on monolayers at water-air interfaces.[44] Moreover, from a fundamental viewpoint, the validity of the dielectric permittivity concept down to a monolayer can be questioned. The nanoscale averaging of lattice polarizability was already discussed in details in the context of multilayered 2D perovskite heterostructures.[25,52] The semi-classical approach presented in this work allows circumventing this difficulty by using a DFT computation at the initial stage.

Conclusions

In summary, we present a theoretical methodology that bridges classical electromagnetism and the outputs of first-principles calculations to relate the change of absolute valence energy levels (or work functions) to the modulation of surface dipoles. We apply the methodology to a variety of systems to demonstrate its power. Furthermore, we show the additivity of the polarization density profiles across heterostructures, which allows us to decipher the interplay between surface dipoles in the readjustment of band alignments in buried interfaces. Overall, this work provides a theoretical strategy to propose, analyze, interpret and fine-tune energy level alignments for designing high-performance optical and optoelectronic devices.

Computational methods

First-principles calculations were performed using SIESTA[53,54] code based on a basis set of finite-range of numerical atomic orbitals. Structural relaxations were peformed using the van der Waals density functional with C09 exchange[55] combined with DF2 flavor.[56] We used the revisited Slater half-occupation technique in the so-called DFT-1/2 implementation in order to correct the band gaps.[57,58] DFT-1/2 was used on top of GGA-PBE[59] functional for the band structure and alignment calculations. Spin-orbit coupling, in its on-site approximation, was included in the computation of the band gaps.[60]

The absolute valence energy levels of the different systems were computed using the Hartree potential alignment with the vacuum level set as the reference.[9,61] Here, the absolute valence energy level E_v^{abs} is obtained using:

$$E_v^{abs} = VBM_{bulk} + \Delta V_H + \Delta E_{vacuum} \tag{14}$$

where E_v^{abs} is the absolute valence energy level, VBM_{bulk} is the valence band maximum of the bulk system, ΔV_H is the shift of the Hartree potential between the slab and the bulk system, and ΔE_{vacuum} is the vacuum level shift. For the absolute energy level of conduction

bands, E_c^{abs}, we calculated it by adding to E_v^{abs} the theoretically computed band gap of the bulk compound within DFT-1/2 giving:

$$E_c^{abs} = E_v^{abs} + E_{g,bulk} \tag{15}$$

Detailed computational methods is provided in the SI.

Supporting Information Available

The supplementary information contains:

More computational details of DFT calculations using SIESTA code;

Computational method of absolute energy alignment;

Absolute valence energy alignment of $CsPbBr_3$ perovskite;

Band structure with Cs surface coating including the Local density of states of surface states;

Layer-by-layer projected density of states of $CsPbI_3$ slab with DMSO at the surfaces;

Band structure and charge transfer from surface passivation with DMSO;

Additivity of the surface dipole for $PEA_2PbI_4/CsPbI_3$ 2D/3D heterostructure.

Acknowledgement

This work was performed with funding from the European Union's Horizon 2020 research and innovation program under grant agreement No. 861985 (PEROCUBE). J.E. acknowledges financial support from the Institute Universitaire de France. This work was granted access to the HPC resources of [TGCC/CINES/IDRIS] under the allocations 2020-A0100911434 and 2020-A0090907682 made by GENCI. B.T. and C.K. thank Dr. S. Tao (Eindhoven University of Technology) for providing the source code of the DFT-1/2 program.

References

(1) The interface is still the device. *Nat. Mater.* **2012**, *11*, 91–91.

(2) Schulz, P.; Cahen, D.; Kahn, A. Halide Perovskites: Is It All about the Interfaces? *Chem. Rev.* **2019**, *119*, 3349–3417.

(3) Canil, L.; Cramer, T.; Fraboni, B.; Ricciarelli, D.; Meggiolaro, D.; Singh, A.; Liu, M.; Rusu, M.; Wolff, C. M.; Phung, N.; Wang, Q.; Neher, D.; Unold, T.; Vivo, P.; Gagliardi, A.; De Angelis, F.; Abate, A. Tuning Halide Perovskite Energy Levels. *Energy Environ. Sci.* **2021**, *14*, 1429–1438.

(4) Xue, J.; Wang, R.; Chen, X.; Yao, C.; Jin, X.; Wang, K.-L.; Huang, W.; Huang, T.; Zhao, Y.; Zhai, Y.; Meng, D.; Tan, S.; Liu, R.; Wang, Z.-K.; Zhu, C.; Zhu, K.; Beard, M. C.; Yan, Y.; Yang, Y. Reconfiguring The Band-edge States of Photovoltaic Perovskites by Conjugated Organic Cations. *Science* **2021**, *371*, 636–640.

(5) Heimel, G.; Romaner, L.; Zojer, E.; Brédas, J.-L. A Theoretical View on Self-Assembled Monolayers in Organic Electronic Devices. *Proc SPIE* **2008**, *6999*, 699919–1.

(6) Helander, M.; Wang, Z.; Qiu, J.; Greiner, M.; Puzzo, D.; Liu, Z.; Lu, Z. Chlorinated Indium Tin Oxide Electrodes with High Work Function for Organic Device Compatibility. *Science* **2011**, *332*, 944–7.

(7) Yajima, T.; Hikita, Y.; Minohara, M.; Bell, C.; Mundy, J.; Kourkoutis, L.; Muller, D.; Kumigashira, H.; Oshima, M.; Hwang, H. Controlling Band Alignments by Artificial Interface Dipoles at Perovskite Heterointerfaces. *Nat. Commun.* **2015**, *6*, 6759.

(8) Zheng, Y.; Fang, Z.; Shang, M.; Sun, Q.; Zheng, J.; Yang, Z.; Hou, X.; Yang, W. Linearly Tailored Work Function of Orthorhombic CsSnI3 Perovskites. *ACS Energy Lett.* **2021**, *6*, 2328–2335.

(9) Lodeiro, L.; Barría-Cáceres, F.; Jiménez, K.; Contreras, R.; Montero-Alejo, A. L.; Menéndez-Proupin, E. Methodological Issues in First-Principle Calculations of $CH_3NH_3PbI_3$ Perovskite Surfaces: Quantum Confinement and Thermal Motion. *ACS Omega* **2020**, *5*, 29477–29491.

(10) Kojima, A.; Teshima, K.; Shirai, Y.; Miyasaka, T. Organometal Halide Perovskites as Visible-Light Sensitizers for Photovoltaic Cells. *J. Am. Chem. Soc.* **2009**, *131*, 6050–6051.

(11) Lee, M. M.; Teuscher, J.; Miyasaka, T.; Murakami, T. N.; Snaith, H. J. Efficient Hybrid Solar Cells Based on Meso-Superstructured Organometal Halide Perovskites. *Science* **2012**, *338*, 643–647.

(12) `https://www.nrel.gov/pv/cell-efficiency.html`, Accessed: 07-07-2021.

(13) Duan, J.; Wang, M.; Wang, Y.; Zhang, J.; Guo, Q.; Zhang, Q.; Duan, Y.; Tang, Q. Effect of Side-Group-Regulated Dipolar Passivating Molecules on CsPbBr3 Perovskite Solar Cells. *ACS Energy Lett.* **2021**, *6*, 2336–2342.

(14) Meggiolaro, D.; Mosconi, E.; Proppe, A. H.; Quintero-Bermudez, R.; Kelley, S. O.; Sargent, E. H.; De Angelis, F. Energy Level Tuning at the $MAPbI_3$ Perovskite/Contact Interface Using Chemical Treatment. *ACS Energy Lett.* **2019**, *4*, 2181–2184.

(15) De Roo, J.; Ibáñez, M.; Geiregat, P.; Nedelcu, G.; Walravens, W.; Maes, J.; Martins, J. C.; Van Driessche, I.; Kovalenko, M. V.; Hens, Z. Highly Dynamic Ligand Binding and Light Absorption Coefficient of Cesium Lead Bromide Perovskite Nanocrystals. *ACS Nano* **2016**, *10*, 2071–2081.

(16) Volonakis, G.; Giustino, F. Ferroelectric Graphene–Perovskite Interfaces. *The Journal of Physical Chemistry Letters* **2015**, *6*, 2496–2502.

(17) Traore, B.; Pedesseau, L.; Blancon, J.-C.; Tretiak, S.; Mohite, A. D.; Even, J.; Katan, C.; Kepenekian, M. Importance of Vacancies and Doping in the Hole-Transporting Nickel Oxide Interface with Halide Perovskites. *ACS Appl. Mater. Interfaces* **2020**, *12*, 6633–6640.

(18) Franciosi, A.; Van de Walle, C. G. Heterojunction band offset engineering. *Surf. Sci. Rep.* **1996**, *25*, 1–140.

(19) Yang, C.; Wang, H.; Miao, Y.; Chen, C.; Zhai, M.; Bao, Q.; Ding, X.; Yang, X.; Cheng, M. Interfacial Molecular Doping and Energy Level Alignment Regulation for Perovskite Solar Cells with Efficiency Exceeding 23%. *ACS Energy Letters* **2021**, *6*, 2690–2696.

(20) Noel, N. K.; Abate, A.; Stranks, S. D.; Parrott, E. S.; Burlakov, V. M.; Goriely, A.; Snaith, H. J. Enhanced Photoluminescence and Solar Cell Performance via Lewis Base Passivation of Organic–Inorganic Lead Halide Perovskites. *ACS Nano* **2014**, *8*, 9815–9821.

(21) Béchu, S.; Ralaiarisoa, M.; Etcheberry, A.; Schulz, P. Photoemission Spectroscopy Characterization of Halide Perovskites. *Adv. Energy Mater.* **2020**, *10*, 1904007.

(22) Leung, T. C.; Kao, C. L.; Su, W. S.; Feng, Y. J.; Chan, C. T. Relationship Between Surface Dipole, Work Function and Charge Transfer: Some Exceptions to An Established Rule. *Phys. Rev. B* **2003**, *68*, 195408.

(23) Even, J.; Pedesseau, L.; Katan, C. Understanding Quantum Confinement of Charge Carriers in Layered 2D Hybrid Perovskites. *ChemPhysChem* **2014**, *15*, 3733–3741.

(24) Sapori, D.; Kepenekian, M.; Pedesseau, L.; Katan, C.; Even, J. Quantum Confinement and Dielectric Profiles of Colloidal Nanoplatelets of Halide Inorganic and Hybrid Organic-Inorganic Perovskites. *Nanoscale* **2016**, *8*, 6369–6378.

(25) Traore, B.; Pedesseau, L.; Assam, L.; Che, X.; Blancon, J.-C.; Tsai, H.; Nie, W.; Stoumpos, C. C.; Kanatzidis, M. G.; Tretiak, S.; Mohite, A. D.; Even, J.; Kepenekian, M.; Katan, C. Composite Nature of Layered Hybrid Perovskites: Assessment on Quantum and Dielectric Confinements and Band Alignment. *ACS Nano* **2018**, *12*, 3321–3332.

(26) Marronnier, A.; Roma, G.; Boyer-Richard, S.; Pedesseau, L.; Jancu, J.-M.; Bonnassieux, Y.; Katan, C.; Stoumpos, C. C.; Kanatzidis, M. G.; Even, J. Anharmonicity and Disorder in the Black Phases of Cesium Lead Iodide Used for Stable Inorganic Perovskite Solar Cells. *ACS Nano* **2018**, *12*, 3477–3486.

(27) Baikie, T.; Fang, Y.; Kadro, J. M.; Schreyer, M.; Wei, F.; Mhaisalkar, S. G.; Grätzel, M.; White, T. J. Synthesis and Crystal Chemistry of The Hybrid Perovskite $CH_3NH_3PbI_3$ For Solid-State Sensitised Solar Cell Applications. *J. Mater. Chem. A* **2013**, *1*, 5628–5641.

(28) Baum, A.; Schneider, J.; Pease, R. High-Performance Negative Electron Affinity Photocathodes For High Resolution Electron Beam Lithography and Metrology. Proceedings of International Electron Devices Meeting. 1995; pp 409–412.

(29) Liu, F.; Sidhik, S.; Hoffbauer, M.; Lewis, S.; Neukirch, A.; Pavlenko, V.; Tsai, H.; Nie, W.; Even, J.; Tretiak, S.; Ajayan, P.; Kanatzidis, M.; Crochet, J.; Moody, N.; Blancon, J.-C.; Mohite, A. Highly Efficient Photoelectric Effect in Halide Perovskites For Regenerative Electron Sources. *Nat. Commun.* **2021**, *12*.

(30) Lewis, S. G.; Ghosh, D.; Jensen, K. L.; Finkenstadt, D.; Shabaev, A.; Lambrakos, S. G.; Liu, F.; Nie, W.; Blancon, J.-C.; Zhou, L.; Crochet, J. J.; Moody, N.; Mohite, A. D.; Tretiak, S.; Neukirch, A. J. Cesium-Coated Halide Perovskites as a Photocathode Material: Modeling Insights. *J. Phys. Chem. Lett.* **2021**, *12*, 6269–6276.

(31) Lu, H.; Krishna, A.; Zakeeruddin, S. M.; Grätzel, M.; Hagfeldt, A. Compositional And Interface Engineering of Organic-Inorganic Lead Halide Perovskite Solar Cells. *iScience* **2020**, *23*, 101359.

(32) Kim, J.; Ho-Baillie, A.; Huang, S. Review of Novel Passivation Techniques for Efficient and Stable Perovskite Solar Cells. *Solar RRL* **2019**, *3*, 1800302.

(33) Zhao, P.; Kim, B. J.; Jung, H. Passivation in Perovskite Solar Cells: A Review. *Mater. Today Energy* **2018**, *7*, 267–286.

(34) Hills-Kimball, K.; Yang, H.; Cai, T.; Wang, J.; Chen, O. Recent Advances in Ligand Design and Engineering in Lead Halide Perovskite Nanocrystals. *Adv. Science* **2021**, *8*, 2100214.

(35) Nenon, D. P.; Pressler, K.; Kang, J.; Koscher, B. A.; Olshansky, J. H.; Osowiecki, W. T.; Koc, M. A.; Wang, L.-W.; Alivisatos, A. P. Design Principles for Trap-Free $CsPbX_3$ Nanocrystals: Enumerating and Eliminating Surface Halide Vacancies with Softer Lewis Bases. *J. Amer. Chem. Soc.* **2018**, *140*, 17760–17772.

(36) Zhang, H.; Nazeeruddin, M. K.; Choy, W. C. H. Perovskite Photovoltaics: The Significant Role of Ligands in Film Formation, Passivation, and Stability. *Adv. Mater.* **2019**, *31*, 1805702.

(37) Godding, J.; Ramadan, A. J.; Lin, Y.-H.; Schutt, K.; Snaith, H. J.; Wenger, B. Oxidative Passivation of Metal Halide Perovskites. *Joule* **2019**, *3*, 2716–2731.

(38) Fu, L.; Li, H.; Wang, L.; Yin, R.; Li, B.; Yin, L. Defect Passivation Strategies in Perovskites For an Enhanced Photovoltaic Performance. *Energy Environ. Sci.* **2020**, *13*, 4017–4056.

(39) Ahn, N.; Son, D.-Y.; Jang, I.-H.; Kang, S. M.; Choi, M.; Park, N.-G. Highly Reproducible Perovskite Solar Cells with Average Efficiency of 18.3% and Best Efficiency of 19.7% Fabricated via Lewis Base Adduct of Lead(II) Iodide. *J. Amer. Chem. Soc.* **2015**, *137*, 8696–8699.

(40) Vidal, R.; Alberola-Borràs, J.-A.; Habisreutinger, S.; Gimeno-Molina, J.-L.; Moore, D.; Schloemer, T. H.; Mora-Seró, I.; Berry, J.; Luther, J. Assessing Health and Environmental Impacts of Solvents for Producing Perovskite Solar Cells. *Nat. Sustain.* **2021**, *4*, 277–285.

(41) Petrov, A. A.; Fateev, S. A.; Khrustalev, V. N.; Li, Y.; Dorovatovskii, P. V.; Zubavichus, Y. V.; Goodilin, E. A.; Tarasov, A. B. Formamidinium Haloplumbate Intermediates: The Missing Link in a Chain of Hybrid Perovskites Crystallization. *Chem. Mater.* **2020**, *32*, 7739–7745.

(42) Itoh, S.; Ohtaki, H. A Study of The Liquid Structure of Dimethyl Sulfoxide by the X-Ray Diffraction. *Zeitschrift für Naturforschung A* **1987**, *42*, 858–862.

(43) Demchak, R. J.; Fort, T. Surface Dipole Moments of Close-Packed Un-ionized Monolayers at The Air-Water Interface. *J. Colloid Interface Sci.* **1974**, *46*, 191–202.

(44) Oliveira, O. N.; Taylor, D. M.; Lewis, T. J.; Salvagno, S.; Stirling, C. J. M. Estimation of Group Dipole Moments From Surface Potential Measurements on Langmuir Monolayers. *J. Chem. Soc., Faraday Trans. 1* **1989**, *85*, 1009–1018.

(45) Petrov, J. G.; Polymeropoulos, E. E.; Möhwald, H. Three-Capacitor Model for Surface Potential of Insoluble Monolayers. *J. Phys. Chem.* **1996**, *100*, 9860–9869.

(46) Nüesch, F.; Carrara, M.; Zuppiroli, L. Solution versus Vapor Growth of Dipolar Layers on Activated Oxide Substrates. *Langmuir* **2003**, *19*, 4871–4875.

(47) Krüger, J.; Bach, U.; Grätzel, M. Modification of TiO_2 Heterojunctions with Benzoic Acid Derivatives in Hybrid Molecular Solid-State Devices. *Adv. Mater.* **2000**, *12*, 447–451.

(48) Goh, C.; Scully, S. R.; McGehee, M. D. Effects of Molecular Interface Modification in Hybrid Organic-Inorganic Photovoltaic Cells. *J. Appl. Phys.* **2007**, *101*, 114503.

(49) Otálvaro, D.; Veening, T.; Brocks, G. Self-Assembled Monolayer Induced Au(111) and Ag(111) Reconstructions: Work Functions and Interface Dipole Formation. *J. Phys. Chem. C* **2012**, *116*, 7826–7837.

(50) Zhu, T.; Su, J.; Alvarez, J.; Lefèvre, G.; Labat, F.; Ciofini, I.; Pauporté, T. Response Enhancement of Self-Powered Visible-Blind UV Photodetectors by Nanostructured Heterointerface Engineering. *Adv. Funct. Mater.* **2019**, *29*, 1903981.

(51) Davies, J. T.; Rideal, S. E. Interfacial Potentials. *Can. J. Chem.* **1955**, *33*, 947–960.

(52) Katan, C.; Mercier, N.; Even, J. Quantum and Dielectric Confinement Effects in Lower-Dimensional Hybrid Perovskite Semiconductors. *Chem. Rev.* **2019**, *119*, 3140–3192.

(53) Soler, M.; Artacho, E.; Gale, J. D.; Garc, A.; Junquera, J.; Ordejon, P.; Daniel, S. The SIESTA Method for Ab Initio Order-N Materials. *J. Phys.: Condens. Matter* **2002**, *14*, 2745–2779.

(54) Artacho, E.; Anglada, E.; Diéguez, O.; Gale, J. D.; García, A.; Junquera, J.; Martin, R. M.; Ordejón, P.; Pruneda, J. M.; Sánchez-Portal, D.; Soler, J. M. The SIESTA method; developments and applicability. *J. Phys.: Condens. Matter* **2008**, *20*, 064208.

(55) Cooper, V. R. Van der Waals Density Functional: An Appropriate Exchange Functional. *Phys. Rev. B* **2010**, *81*, 161104.

(56) Hamada, I.; Otani, M. Comparative Van Der Waals Density-Functional Study of Graphene on Metal Surfaces. *Phys. Rev. B* **2010**, *82*, 153412.

(57) Ferreira, L. G.; Marques, M.; Teles, L. K. Approximation to Density Functional Theory For The Calculation of Band Gaps of Semiconductors. *Phys. Rev. B* **2008**, *78*, 125116.

(58) Tao, S. X.; Cao, X.; Bobbert, P. A. Accurate And Efficient Band Gap Predictions of Metal Halide Perovskites Using The DFT-1/2 Method: GW Accuracy With DFT Expense. *Sci. Rep.* **2017**, *7*, 14386.

(59) Perdew, J. P.; Burke, K.; Ernzerhof, M. Generalized Gradient Approximation Made Simple. *Phys. Rev. Lett.* **1996**, *77*, 3865–3868.

(60) Fernández-Seivane, L.; Oliveira, M. A.; Sanvito, S.; Ferrer, J. On-site approximation for spin–orbit coupling in linear combination of atomic orbitals density functional methods. *J. Phys.: Condens. Matter* **2006**, *18*, 7999–8013.

(61) Das, T.; Rocquefelte, X.; Jobic, S. Ab Initio Positioning of the Valence and Conduction Bands of Bulk Photocatalysts: Proposition of Absolute Reference Energy. *J. Phys. Chem. C* **2020**, *124*, 19426–19434.

A theoretical framework for microscopic surface and interface dipoles, work functions and valence band alignments in 2D and 3D halide perovskite heterostructures

Supplementary Information

Boubacar Traore,*[1] Pooja Basera,[1,2] Alexandra J. Ramadan,[3] Henry J. Snaith,[3] Claudine Katan,[1] and Jacky Even*[2]

[1] *Univ Rennes, ENSCR, INSA Rennes, CNRS, ISCR - UMR 6226, F-35000 Rennes, France.*

[2] *Univ Rennes, INSA Rennes, CNRS, Institut FOTON - UMR 6082, F-35000 Rennes, France.*

[3] *Clarendon Laboratory, Department of Physics, University of Oxford, Oxford, United Kingdom*

E-mail: boubacar.traore@univ-rennes1.fr

jacky.even@insa-rennes.fr

Contents

Text S1 | Computational details for localized basis-sets calculations (SIESTA)

DFT-based calculations[1,2] were performed using SIESTA[3,4] using a basis set of finite-range of numerical atomic orbitals. For structural optimization, we used the van der Waals density functional with C09 exchange[5] within the van der Waals DF2 flavor to describe the exchange-correlation term (we modified SIESTA version "master-post-4.1-251" to include DF2 flavor). This tuning was suggested to improve C09 based geometry optimization over that with the original DF1 flavor[6]. The latter has already proven to provide a good description of experimental lattice constants similar to those obtained with optimized GGA based PBEsol functional in solids.[7,8]. Norm-conserving Troullier-Martins pseudopotentials were used for each atomic species to account for the core electrons.[9] $1s^1$, $2s^22p^2$, $2s^22p^3$, $5s^25p^5$, $5d^{10}6s^26p^2$, $2s^22p^4$ and $3s^23p^4$ were used as valence electrons for H, C, N, I, Pb, O and S respectively. Polarized Double-ζ (DZP) basis set with an energy shift of 200 meV and a real space mesh grid energy cutoff of 300 Rydberg were used for the calculations. We used 8x8x8 and 6x6x1 Monkhorst-Pack k-point grids for the bulk and slab systems, respectively. For $CsPbI_3$ slabs, we doubled the cells along a-b planes resulting in lattice constants equal to that of the bulk multiplied by $\sqrt{2}$ ($a_{slab} = \sqrt{2} \times a_{bulk}$).

For band structures, band alignments and charge densities for polarization density profiles, we used single-point calculations with GGA-PBE[10] functional combined with DFT-1/2[11] including spin-orbit coupling on top of vdwDF2-C09 optimized structures. Spin-orbit coupling (SOC), when used, was considered in its on-site approximation as proposed by Fernández-Seivane *et al*[12].

To compute the polarization density profiles, we removed the spurious "unphysical" charge densities beyond 30 Bohr from the surface deep inside the vacuum. Since, so far, SIESTA does not keep symmetries from geometry optimizations, we also take the half-sum of the total charge densities across the slab in forward and reverse directions resulting in a more symmetrized density profile ($e.g.: \rho[1:n] = 0.5 \times (\rho[1:1:n] + \rho[n:-1:1])$ where n is the size the charge density array ρ along z). This to reflect the symmetry of the surfaces by construction and has only minor effects on the results.

Structural relaxation

The fully relaxed bulk structures were used to construct the slabs. With the slabs constructed, only the atomic positions were allowed to relax when surface layers relaxation was requested. We only allowed the two surface octahedral layers of the perovskite to relax while keeping the bulk-like regions frozen to the positions of the optimized bulk structure. This strategy allows capture of the surface effects during the relaxation while maintaining the integrity of the bulk region of the slabs, which is useful for the energy level alignment. We used the fast inertial relaxation engine (FIRE) algorithm[13] for the different relaxations and the maximum force was set to 0.04 eV/Å. We used 10 octahedral layers to construct the different slabs since we found that this thickness was sufficient for converged absolute valence energy levels. For the PbI_2 terminated surface, we had 9 effective octahedral layers due to the removal of surface CsI atoms to obtain PbI_2 termination. The same applies for $CsPbBr_3$ slabs (*vide infra*)

Structural information

For the structures, we used the pseudo-cubic structure of $CsPbI_3$ generated from its room-temperature orthorhombic cell as reported in Ref.[14]. The lattice constant of this pseudo-cubic structure was obtained using : $a_{pseudocubic} = (V_{ortho}/4)^{1/3}$, where V_{ortho} is the volume of the room-temperature orthorhombic cell. Similarly, for $CsPbBr_3$, we used the pseudo-cubic structure from its room-temperature orthorhombic cell[15].

2D/3D heterostructure construction

We used the doubled pseudo-cubic cells in the plane of the perovskite to lattice match it to the 2D layer cell. This cell doubling corresponds to multiplying the pseudo-cubic lattice constant by $\sqrt{2}$. For the heterostructure using 2D based BA, we used the room temperature structure of BA_2PbI_4 as reported in Ref.[16]. As for PEA, we used the structure recorded at 295K from Ref.[17]. We considered 9 octahedral layers of $CsPbI_3$ to mimic the 3D part of the heterostructure. The in-plane lattice constants of the 3D part were imposed for the whole heterostructure and were not allowed to relax during the 2D/3D interface geometry optimization. We only allowed the c-lattice constant along z to relax along with the atomic positions.

Note on slab dipole correction

In modeling slabs with asymmetric surface terminations, an artificial electric field is created across the slab due to the periodic boundary conditions. This is reflected as a potential slope in the vacuum region of the slab. Quite often a dipole correction scheme is imposed to compensate for the artificial electric field[18,19] and thus making the potential flat in the vacuum region. This would then allow to compute quantities such as work functions with asymmetric surface terminations. Here, we used symmetrically terminated slab surfaces by construction such that there is negligible potential slope in the vacuum region and that there is no need to use any dipole correction scheme. We checked that the dipole correction has negligible effects on the absolute valence energy levels with our symmetric surface terminations. In addition the symmetric termination is desired in our approach in order to reliably extract the surface dipoles from the developed methodology.

Band gap correction

Since normal DFT severely underestimates the bandgap, we used the revisited Slater half-occupation technique in the so-called DFT-1/2 implementation in order to correct the band gaps[11,20]. This technique allows to obtain reasonable band gaps in good agreement with experiments and at a much computationally affordable cost. For DFT-1/2 correction, we removed $1/2e^-$from p and s orbitals of halides and lead (Pb) atoms, respectively. This is because the valence band maximum of these halide perovskites is made of an anti-bonding hybridization between Pb (s) and halides (p) states[21]. We note that spin-orbit coupling effect was included.

Charge transfer

The charge transfer from the adsorbate to the slab or vice-versa was computed using:

$$\Delta\rho = \rho_{slab+adsorb} - (\rho_{slab} + \rho_{adsorb}) \tag{1}$$

where $\Delta\rho$ is the charger transfer from or to the perosvkite slab, $\rho_{slab+adsorb}$ is charge density of the whole system including the perovskite and the adsorbate layers, ρ_{slab} is the charge density of the perovskite part of the slab and ρ_{adsorb} is the charge density of the adsorbate or added foreign layer. Here, a positive value of $\Delta\rho$ corresponds to electronic charge accumulation while a negative value corresponds to electronic charge depletion. Note that within SIESTA convention for total charge density: a positive sign is for electronic charge density and a negative sign is for ionic charge density.

Text S2 | The computation of absolute valence energy levels

The absolute valence energy levels of the different systems were computed using the Hartree potential alignment with the vacuum level set as the reference[22,23]. Here, the absolute valence energy level E_v^{abs} is obtained using:

$$E_v^{abs} = VBM_{bulk} + \Delta V_H + \Delta E_{vacuum} \tag{2}$$

where VBM_{bulk} is the valence band maximum of the bulk system, $\Delta V_H = V_H^{slab} - V_H^{bulk}$ is the shift of the Hartree potential between the slab and the bulk systems, and $\Delta E_{vacuum} = 0 - E_{vacumm}$ is the vacuum level shift with respect to zero energy level. For the conduction band, we added to E_v^{abs} the theoretically computed band gap of the bulk compound using DFT-1/2. This then gives,

$$E_c^{abs} = E_v^{abs} + E_{g,bulk} \tag{3}$$

Text S3 | $MAPbI_3$ relaxed structures

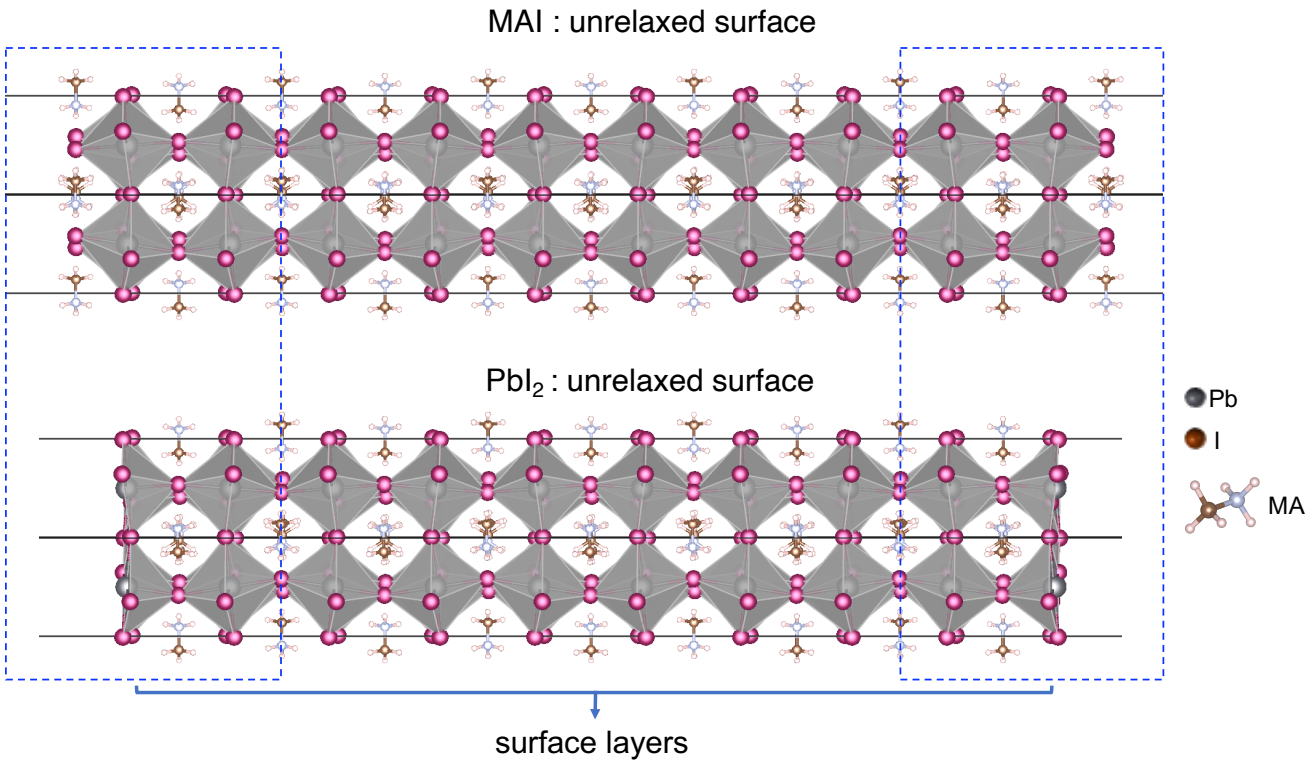

Figure S1 | Structures of $MAPbI_3$ slabs with the relaxed surface layers considering both MAI and PbI_2 terminations.

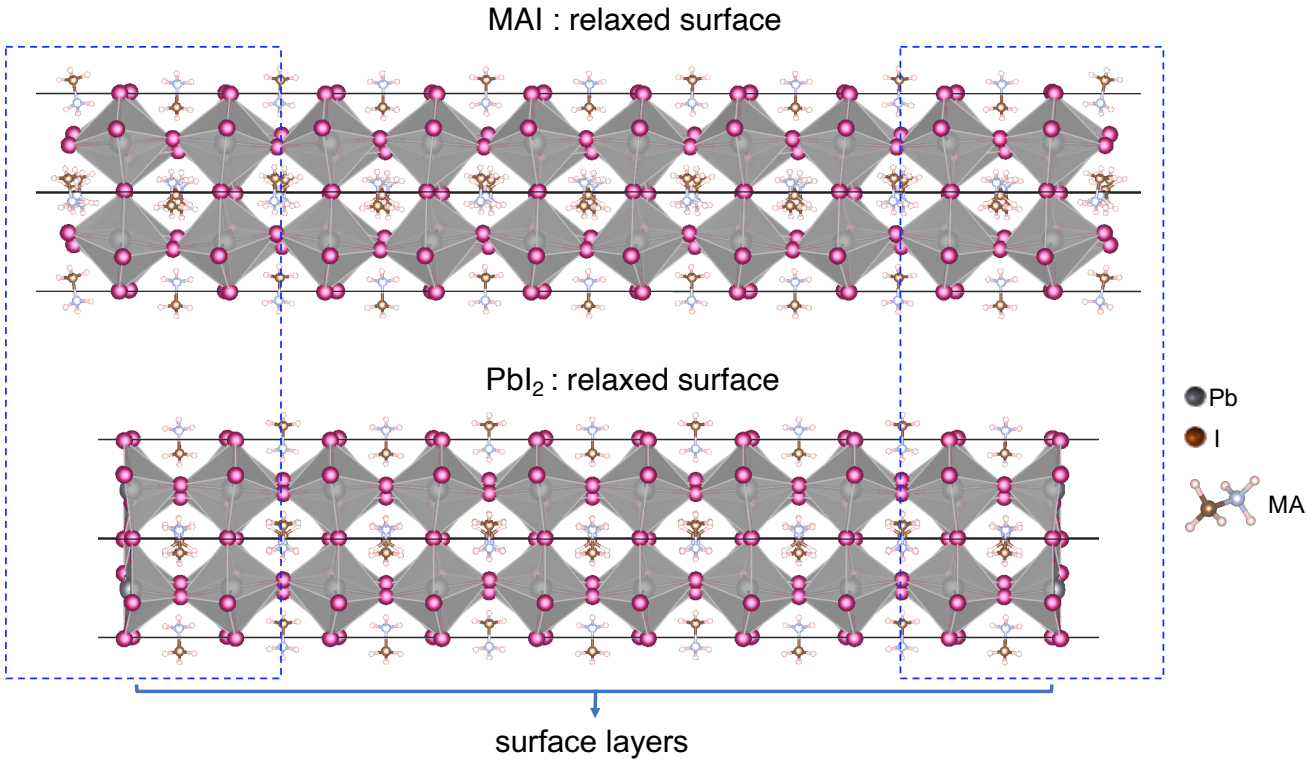

Figure S2 | Structures of $MAPbI_3$ slabs with the relaxed surface layers considering both MAI and PbI_2 terminations.

Text S4 | Absolute valence energy alignment of $CsPbBr_3$ perovskite

This section compares the absolute valence energy alignment of $CsPbBr_3$ slabs with the surface layers unrelaxed (Figure **S3**) or relaxed (Figure **S4**). Similar to $CsPbI_3$, the trend of E_v^{abs} between CsBr and $PbBr_2$ terminated surfaces is reversed when the surface layers are relaxed as compared to the unrelaxed ones. In the unrelaxed case, E_v^{abs} is deeper for the $PbBr_2$ terminated surface as compared to CsBr by about 2.2 eV and this is due to the larger surface dipole for the $PbBr_2$ terminated surface (Figure **S3**c). Notably, the difference of 2.2 eV in E_v^{abs} is in excellent agreement with $\Delta\phi$ (-2.20 eV) computed from the difference of the surface dipole moments. For the relaxed surface layers, E_v^{abs} is deeper for the CsBr terminated surface as compared to $PbBr_2$ by about 1.03 eV. Again, this difference in nicely captured by the larger surface dipole of the CsBr-terminated surface as a result of surface relaxation (Figure **S4**c). By computing $\Delta\phi$ (+1.08 eV) using Eq. (10) of the main text, we observe an excellent agreement with ΔE_v^{abs} (+1.03 eV). Table **S1** summarizes the computed absolute valence energy levels along with the difference of the surface dipoles for the various cases of $CsPbBr_3$ slabs.

Table S1 | Comparison of absolute valence energy levels (E_v^{abs}) calculated for the different systems. The table also compares the shifts of absolute valence energy levels obtained from the difference of surface dipoles ($\Delta\phi$ using Eq 10 of the main text) and those computed from the Hatree potential alignment (Figure 2b and Eq. 14 of the main text). CsBr-termination is taken as the reference.

Unrelaxed surface layers				
	$E_v^{abs} = \phi$ (eV)	ΔE_v^{abs} (eV)	Δp (C/m)	$\Delta\phi$ (eV)
CsBr	-4.80	-	-	-
$PbBr_2$	-7.00	-2.20	1.97×10^{-11}	-2.22
Relaxed surface layers				
CsBr	-6.79	-	-	-
$PbBr_2$	-5.76	$+1.03$	-0.96×10^{-11}	$+1.08$

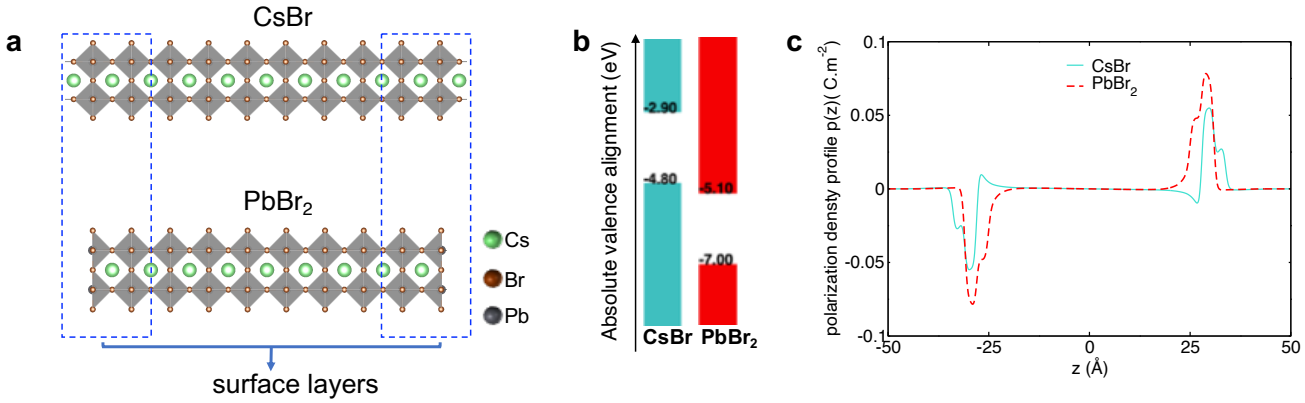

Figure S3 | Effect of surface termination on absolute energy alignments of $CsPbBr_3$ with unrelaxed surface layers. **a** $CsPbBr_3$ structures with CsBr and $PbBr_2$ terminations with unrelaxed surface layers. The surface layers are shown by dashed rectangles on either side of the slab. **b** Computed absolute valence energy levels for CsBr and $PbBr_2$ terminated surfaces, respectively for the unrelaxed surface layers. **c** Polarization density profiles of the two slab systems showing different surface dipoles for the unrelaxed surface layers. The integration of these profiles result in the surface dipole moments.

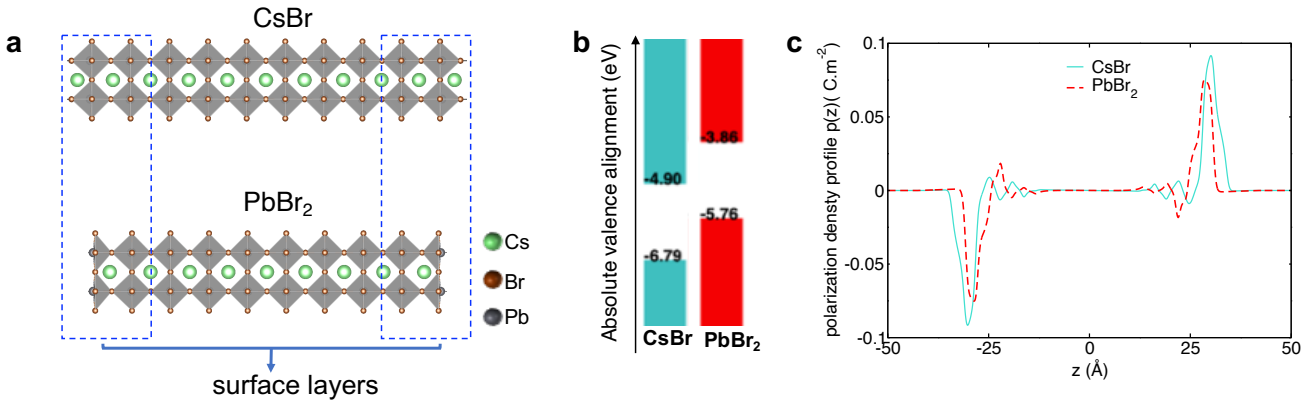

Figure S4 | Effect of surface termination on absolute energy alignments of $CsPbBr_3$ with relaxed surface layers. **a** $CsPbBr_3$ structures with CsBr and $PbBr_2$ terminations with relaxed surface layers. The surface layers are shown by dashed rectangles on either side of the slab. **b** Computed absolute valence energy levels for CsBr and $PbBr_2$ terminated surfaces, respectively for the relaxed surface layers. **c** Polarization density profiles of the two slab systems showing different surface dipoles for the relaxed surface layers. The integration of these profiles result in the surface dipole moments.

Text S5 | Effect of surface relaxation on the absolute valence energy level

Table **S2** compares the variation of the in-plane and out-of-plane PbI bond lengths and Pb-I-Pb angles for the $CsPbI_3$ slabs when the surface layers are unrelaxed and relaxed. The results are shown for both CsI and PbI_2-terminated surfaces. Upon the surface layers relaxation, both the in-plane and out-of-plane PbI bond lengths are stretched for CsI-termination while only the in-plane PbI bond is stretched for PbI_2 termination with the out-of-plane one contracted. However, the main impact of the surface relaxation is seen on the in-plane Pb-I-Pb angles which undergo a dramatic decrease from the ideal 180° for both CsI and PbI_2 terminations. This effect is much larger in CsI termination reaching about twice the variation seen in PbI_2 termination. It is quite establisehd that octahedral distortions have a significant influence on the electronic properties of halide perovskites[24–27]. The valence band maximum (VBM) of these compounds is made of an anti-bonding hybridization between the halide X(p) states and the metal M(s) states. The larger Pb-I-Pb deviation from the ideal 180° in the case of CsI termination leads to much less destabilized X(p) - M(s) coupling, which results in much deeper VBM. In addition, the longer PbI bonds in CsI-termination also exacerbates this less destabilized X(p) - M(s) coupling at the VBM giving rise to its much deeper absolute valence energy level after relaxation. In the case Of PbI_2 termination, the same effect occurs but to a lesser extent. Besides, the shorter out-of-plane PbI bond in PbI_2 after relaxation tends to destabilize X(p) - M(s) coupling which counteracts the deepening of VBM. Thus, its less deeper absolute valence energy level after relaxation as compared to the CsI-termination. Therefore, the change of trend between the relaxed and unrelaxed surfaces for the two terminations is related to the way the two surfaces are reorganized after relaxation which is reflected in the computed surface dipoles.

Table S2 | Comparison of average in-plane and out-of-plane Pb-I-Pb angles, in-plane and out-of-plane PbI bond lengths at the outermost surface layers of $CsPbI_3$ slab. subscripts "in" and "out" refer to the in-plane and out-of-plane, respectively. The percentage variation with respect to the unrelaxed systems are given in parenthesis.

	PbI_{in} (Å)	Pb-I-Pb_{in} (°)	PbI_{out} (Å)	Pb-I-Pb_{out} (°)
Unrelaxed surface layers				
CsI	3.15	180.0	3.15	180
PbI_2	3.15	180.0	3.15	180
Relaxed surface layers				
CsI	3.17 (+0.6%)	165.7 (-7.9%)	3.20 (+1.6%)	180.0 (0.0%)
PbI_2	3.16 (+0.3%)	172.6 (-4.1%)	3.11 (-1.3 %)	180.0 (0.0%)

Table **S3** compares the variation of the in-plane and out-of-plane PbI bond lengths and Pb-I-Pb angles for the $MAPbI_3$ slabs when the surface layers are unrelaxed and relaxed. The results are shown for both MAI and PbI_2-terminated surfaces. Here, the relaxation did not induce significant changes on the average PbI bond lengths and Pb-I-Pb angles for either surface termination. However, the values undergo a noticeable fluctuation between the lower and upper bounds as shown in the table, as a result of the distortions that lead to some deepening of the subsequent absolute valence energy levels. However, no change of the trend is seen between the unrelaxed and relaxed surfaces for the two terminations due to the similar fluctuations and distortions induced for the two

systems.

Table S3 | Comparison of the in-plane and out-of-plane Pb-I-Pb angles, in-plane and out-of-plane PbI bond lengths at the outermost surface layers of $MAPbI_3$ slab. subscripts "in" and "out" refer to the in-plane and out-of-plane, respectively. The range between the lower and upper bounds is rather shown here to show the distortion effects since the average values for the relaxed structures were similar to the unrelaxed ones.

	PbI_{in} (Å)	Pb-I-Pb_{in} (°)	PbI_{out} (Å)	Pb-I-Pb_{out} (°)
Unrelaxed surface layers				
MAI	3.18	146.3	3.23	160.3
PbI_2	3.18	146.3	3.23	160.3
Relaxed surface layers				
MAI	3.14 - 3.22	140.5 - 152.5	3.20 - 3.32	160.2 - 160.5
PbI_2	3.11 - 3.26	142.2 - 150.0	3.08 - 3.20	160.3 - 160.6

Text S6 | Cs surface coating

Figures **S5** and **S6** report the band structures of $CsPbI_3$ slab with relaxed CsI-terminated surface and the slab terminated with a monolayer of Cs, respectively. As can be seen from Figure **S6**, the monolayer of Cs introduce shallow surface states at the conduction band with the Fermi level (E_F) crossing the bands and making the system n-type. From the local density of states (LDOS) shown in Figure **S6**, the bands due to the surface states are indeed localized on Cs monolayers.

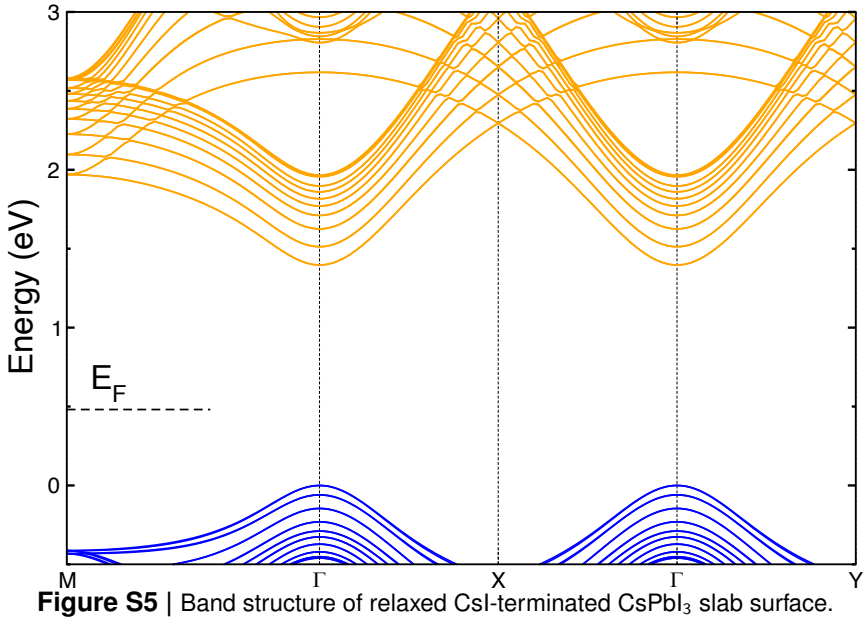

Figure S5 | Band structure of relaxed CsI-terminated $CsPbI_3$ slab surface.

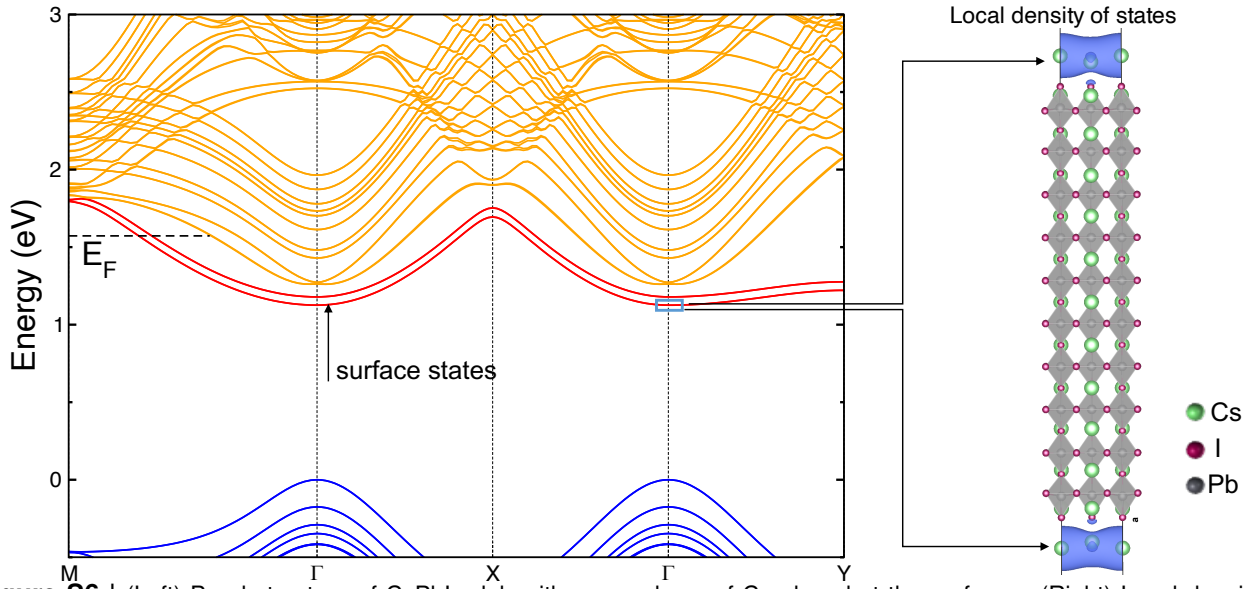

Figure S6 | (Left) Band structure of $CsPbI_3$ slab with a monolayer of Cs placed at the surfaces. (Right) Local density of states (LDOS) of the surface states from the band structure. The LDOS is integrated over an energy window around Γ k-point as shown by the small blue box. The isosurface level is 3.0×10^{-6}.

Text S7 | Surface passivation with DMSO

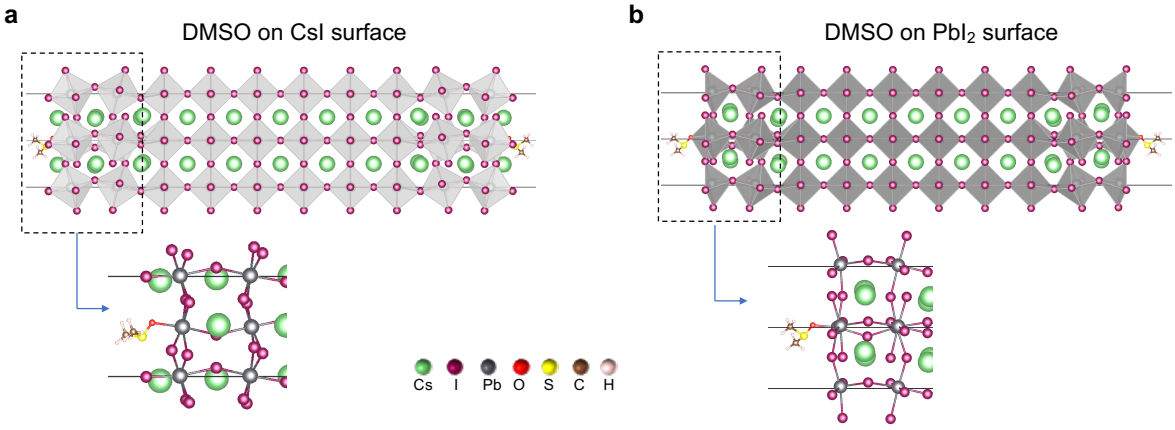

Figure S7 | Relaxed $CsPbI_3$ slabs with DMSO on ' **a** the CsI-terminated surface **b** the PbI_2-terminated surface.

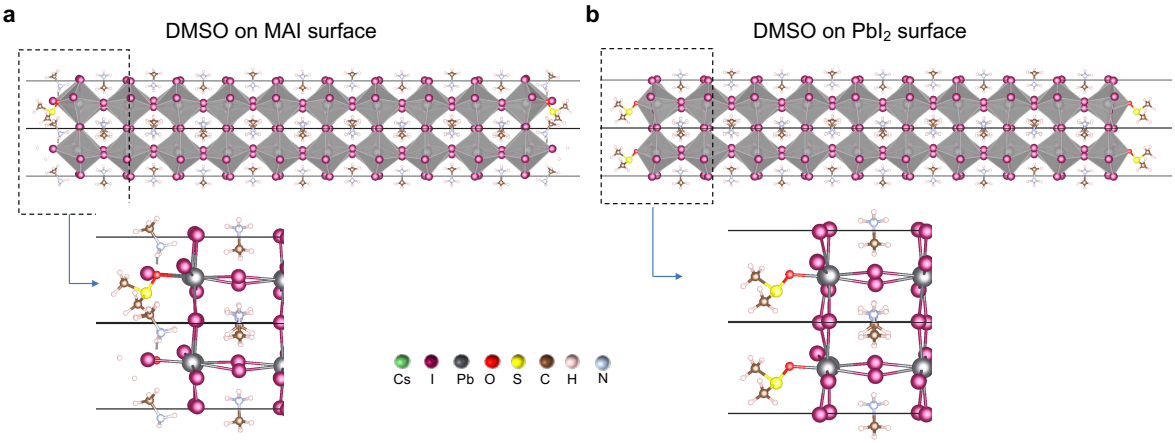

Figure S8 | Relaxed $MAPbI_3$ slabs with DMSO on ' **a** the MAI-terminated surface **b** the PbI_2-terminated surface.

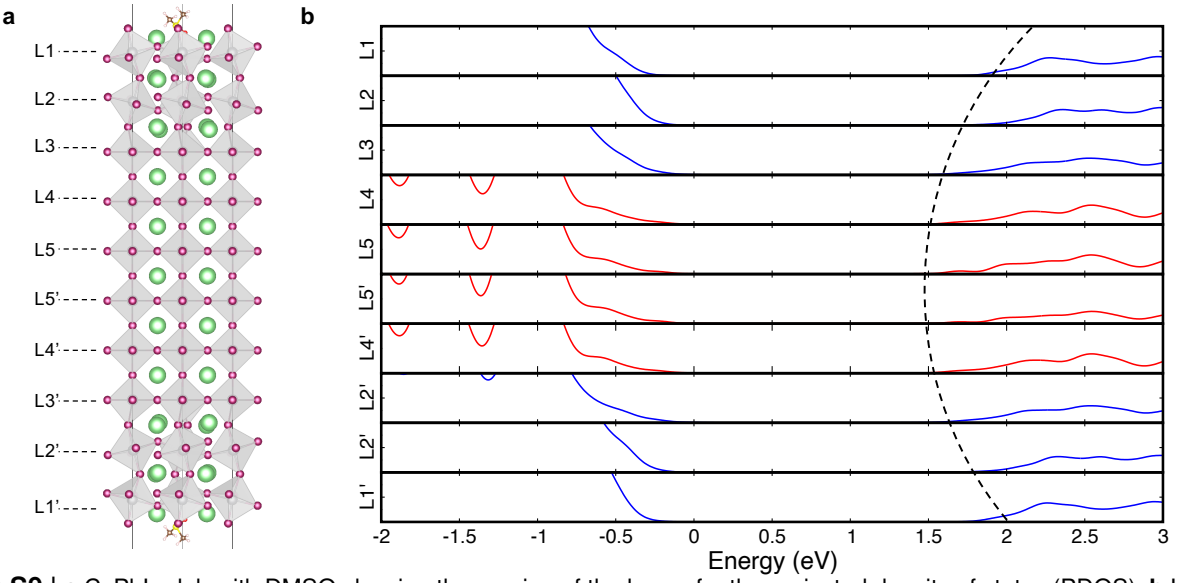

Figure S9 | **a** $CsPbI_3$ slab with DMSO showing the naming of the layers for the projected density of states (PDOS). **b** Layer-by-layer PDOS of $CsPbI_3$ slab with DMSO at the surfaces. PDOS of the inner bulk-like layers are shown in red. The dashed circular arc is a guide to the eye showing the widening of the band gap as one approaches the surface layers. The valence band maximum is set to zero.

Figures **S15** and **S11** compare the band structures of $CsPbI_3$ slab with relaxed CsI-terminated surface and the slab terminated with a DMSO molecule , respectively. As one can see, the two band structures are quite similar and no surface states appear as a result of the introduction of DMSO (Figure **S11**) showing the passivating role of the latter.

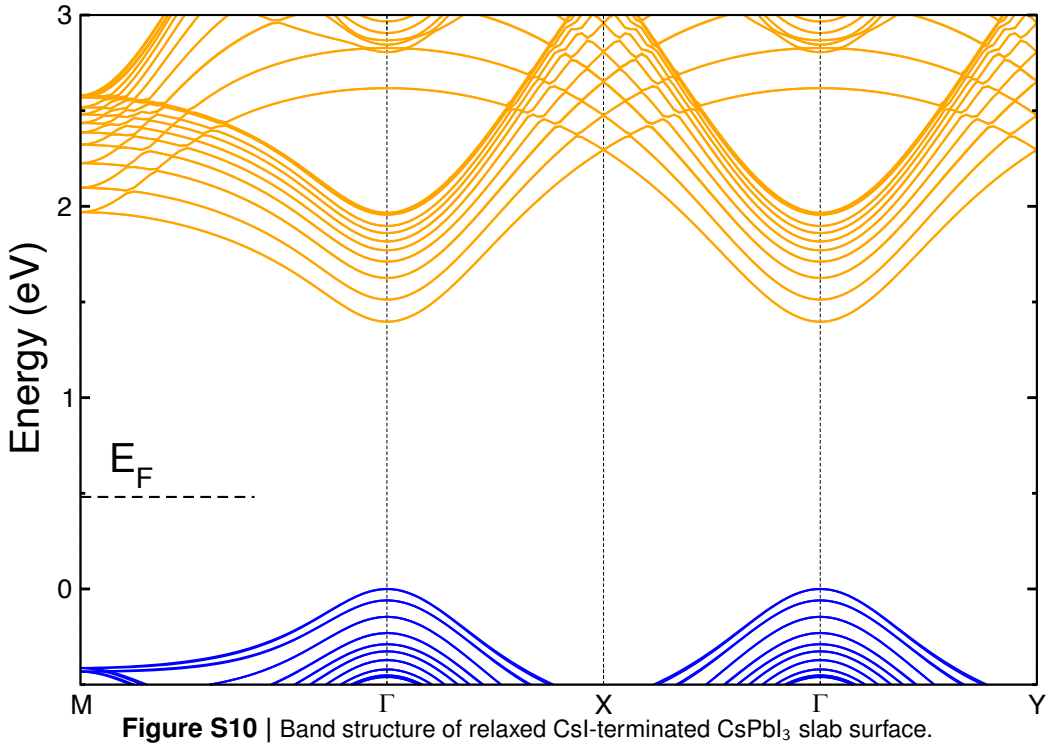

Figure S10 | Band structure of relaxed CsI-terminated $CsPbI_3$ slab surface.

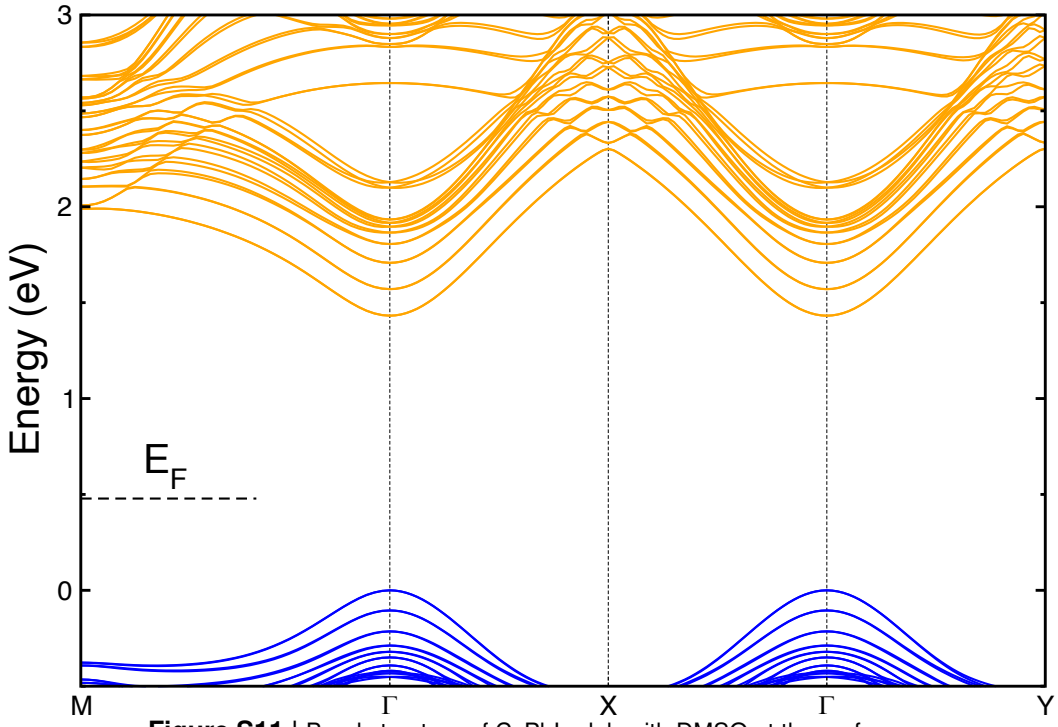

Figure S11 | Band structure of $CsPbI_3$ slab with DMSO at the surfaces.

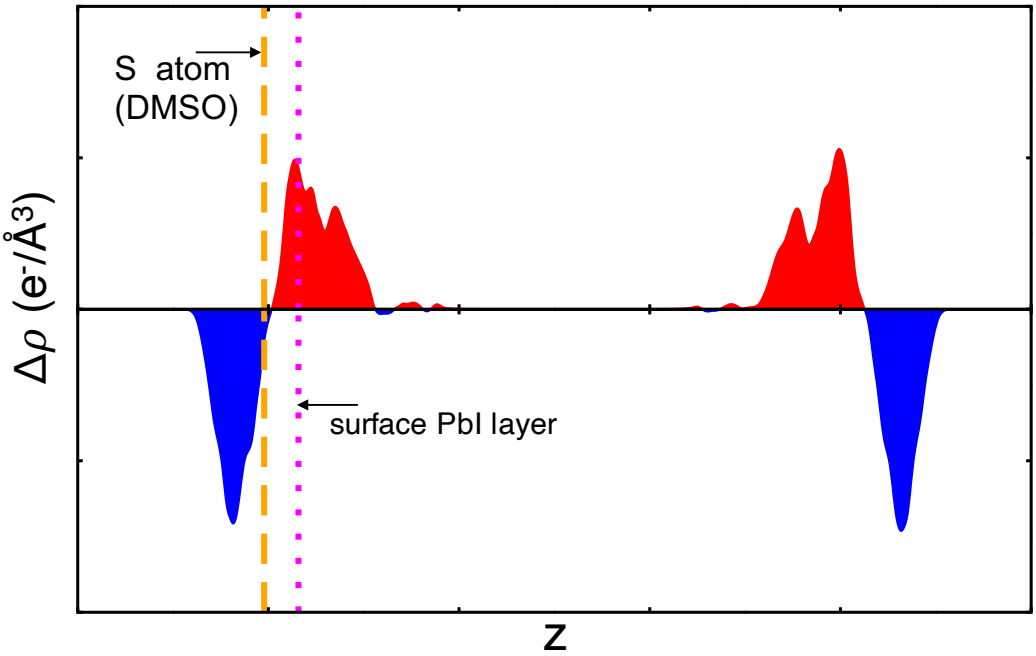

Figure S12 | Profile of total charge density transfered across the slab with DMSO at the surface. Red for electronic charge accumulation and blue for electronic charge depletion. The positions of S atom from DMSO and surface PbI layers are shown by vertical lines. Note that within SIESTA, the convention for total charge densities is: a positive sign is for electronic charge density and a negative sign is for ionic charge density.

Text S8 | Surface passivation with TMPPA

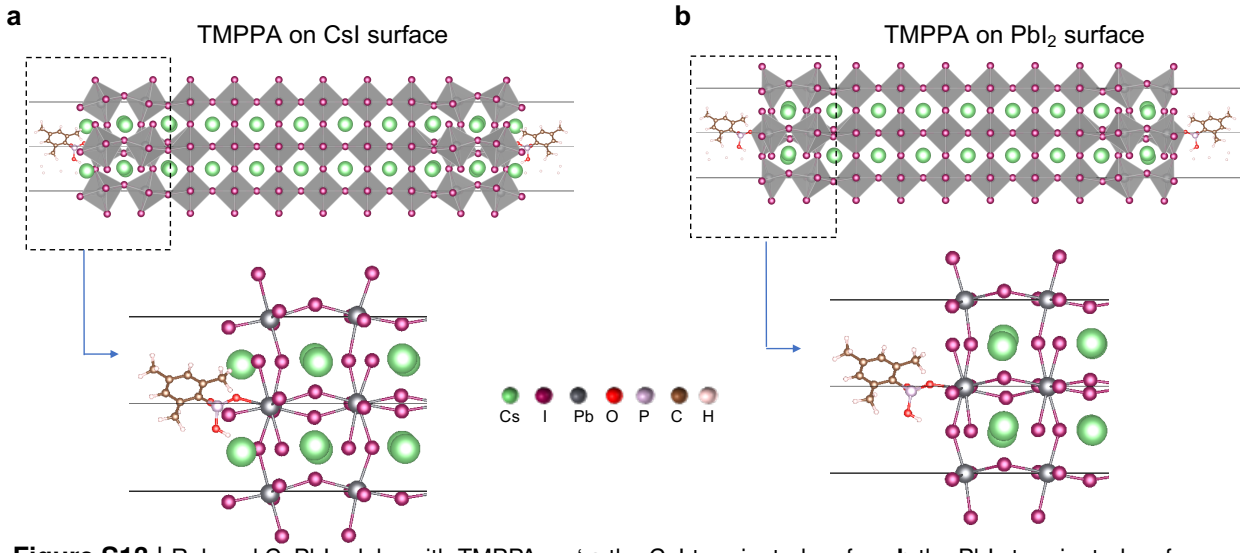

Figure S13 | Relaxed $CsPbI_3$ slabs with TMPPA on ' **a** the CsI-terminated surface **b** the PbI_2-terminated surface.

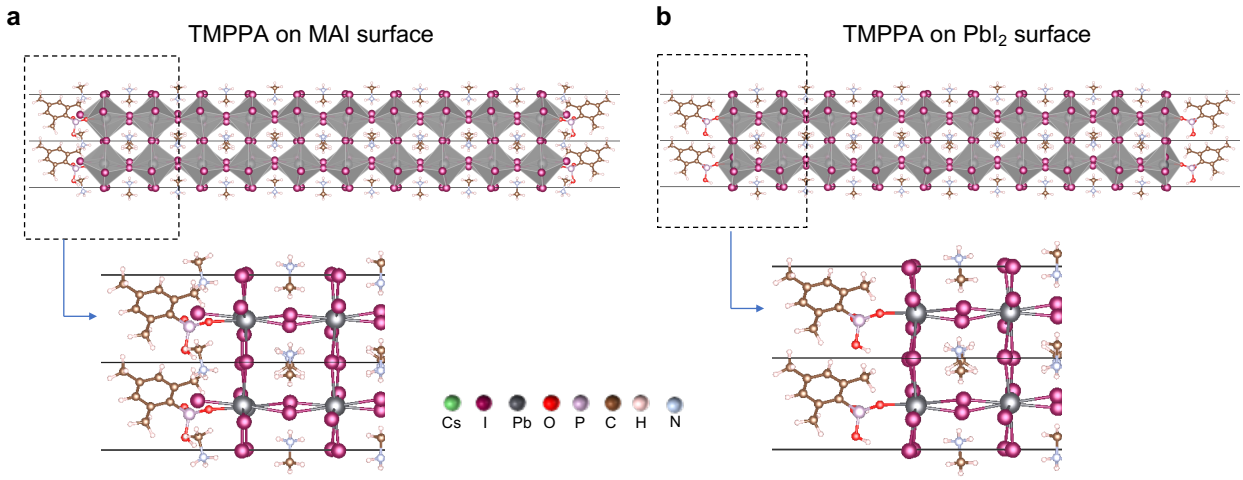

Figure S14 | Relaxed $MAPbI_3$ slabs with TMPPA on ' **a** the MAI-terminated surface **b** the PbI_2-terminated surface.

Figures **S15** and **S16** compare the band structures of $CsPbI_3$ slab with relaxed CsI-terminated surface and the slab terminated with a TMPPA molecule , respectively. As one can see, the two band structures are quite similar and no surface states appear as a result of the introduction of TMPPA (Figure **S11**) showing the passivating role of the latter.

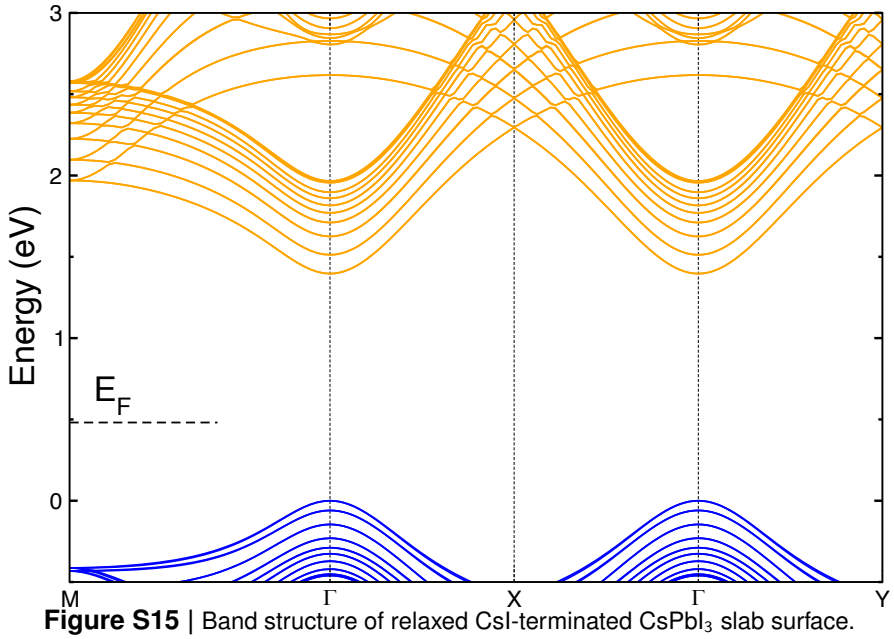

Figure S15 | Band structure of relaxed CsI-terminated $CsPbI_3$ slab surface.

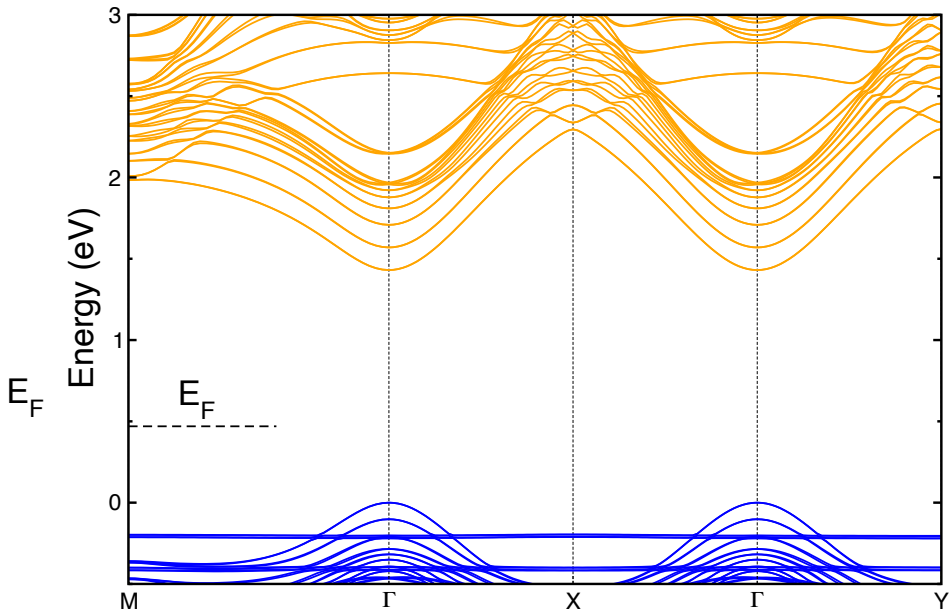

Figure S16 | Band structure of $CsPbI_3$ slab with TMPPA at the surfaces.

Text S9 | Additivity of the surface dipoles in $(PEA)_2PbI_4/CsPbI_3$ heterostructure

Similar to the case of the heterostructure with BA molecule discussed in the main manuscript, one can see the additivity of the surface dipoles with $(PEA)_2PbI_4/CsPbI_3$ heterostructure as well. This indicates the generality of the approach.

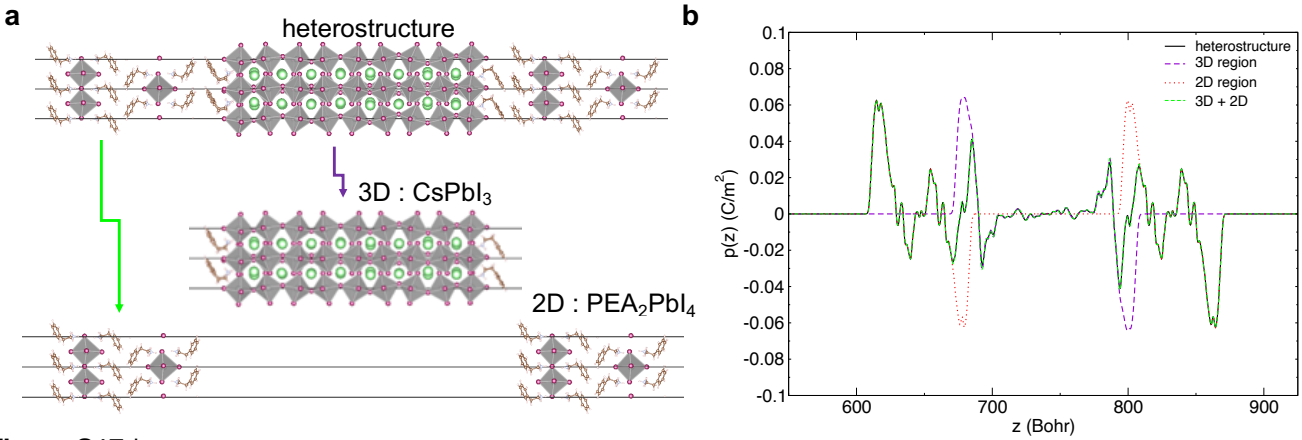

Figure S17 | Additivity of the surface dipoles. **a** The relaxed 2D/3D heterostructure model composed of $CsPbI_3$ interfaced with $(PEA)_2PbI_3$. The heterostructure is viewed as a composite showing its constituent parts. **b** Computed polarization density profiles of the 2D/3D and the constituent parts demonstrating the additivity of the surface dipoles.

References

[1] Hohenberg, P. & Kohn, W. Inhomogeneous electron gas. *Phys. Rev.* **136**, B864–B871 (1964).

[2] Kohn, W. & Sham, L. J. Self-consistent equations including exchange and correlation effects. *Phys. Rev.* **140**, A1133–A1138 (1965).

[3] Soler, M. *et al.* The SIESTA method for ab initio order-N materials. *J. Phys.: Condens. Matter* **14**, 2745–2779 (2002).

[4] Artacho, E. *et al.* The SIESTA method; developments and applicability. *J. Phys.: Condens. Matter* **20**, 064208 (2008).

[5] Cooper, V. R. Van der Waals density functional: An appropriate exchange functional. *Phys. Rev. B* **81**, 161104 (2010).

[6] Hamada, I. & Otani, M. Comparative van der waals density-functional study of graphene on metal surfaces. *Phys. Rev. B* **82**, 153412 (2010).

[7] Yuk, S. F. *et al.* Towards an accurate description of perovskite ferroelectrics: exchange and correlation effects. *Sci. Rep.* **7**, 43482 (2017).

[8] Traore, B. *et al.* Importance of vacancies and doping in the hole-transporting nickel oxide interface with halide perovskites. *ACS Appl. Mater. Interfaces* **12**, 6633–6640 (2020).

[9] Troullier, N. & Martins, J. L. Efficient pseudopotentials for plane-wave calculations. *Phys. Rev. B* **43**, 1993–2006 (1991).

[10] Perdew, J. P., Burke, K. & Ernzerhof, M. Generalized gradient approximation made simple. *Phys. Rev. Lett.* **77**, 3865–3868 (1996).

[11] Ferreira, L. G., Marques, M. & Teles, L. K. Approximation to density functional theory for the calculation of band gaps of semiconductors. *Phys. Rev. B* **78**, 125116 (2008).

[12] Fernández-Seivane, L., Oliveira, M. A., Sanvito, S. & Ferrer, J. On-site approximation for spin–orbit coupling in linear combination of atomic orbitals density functional methods. *J. Phys.: Condens. Matter* **18**, 7999–8013 (2006).

[13] Bitzek, E., Koskinen, P., Gähler, F., Moseler, M. & Gumbsch, P. Structural relaxation made simple. *Phys. Rev. Lett.* **97**, 170201 (2006). URL https://link.aps.org/doi/10.1103/PhysRevLett.97.170201.

[14] Marronnier, A. *et al.* Anharmonicity and disorder in the black phases of cesium lead iodide used for stable inorganic perovskite solar cells. *ACS Nano* **12**, 3477–3486 (2018).

[15] Stoumpos, C. C. *et al.* Crystal growth of the perovskite semiconductor cspbbr$_3$: A new material for high-energy radiation detection. *Cryst. Growth Des.* **13**, 2722–2727 (2013).

[16] Billing, D. & Lemmerer, A. Synthesis, characterization and phase transitions in the inorganic-organic layered perovskite-type hybrids [(cnh$_{2n+1}$nh$_3$)$_2$pbi$_4$], n=4, 5 and 6. *Acta Crystallogr., Sect. B: Struct. Sci.* **63**, 735–47 (2007).

[17] Fang, H.-H. *et al.* Band-edge exciton fine structure and exciton recombination dynamics in single crystals of layered hybrid perovskites. *Adv. Funct. Mater.* **30**, 1907979 (2020).

[18] Bengtsson, L. Dipole correction for surface supercell calculations. *Phys. Rev. B* **59**, 12301–12304 (1999). URL https://link.aps.org/doi/10.1103/PhysRevB.59.12301.

[19] Meyer, B. & Vanderbilt, D. *Ab initio* study of batio$_3$ and pbtio$_3$ surfaces in external electric fields. *Phys. Rev. B* **63**, 205426 (2001).

[20] Tao, S. X., Cao, X. & Bobbert, P. A. Accurate and efficient band gap predictions of metal halide perovskites using the dft-1/2 method: Gw accuracy with dft expense. *Sci. Rep.* **7**, 14386 (2017).

[21] Even, J., Pedesseau, L., Dupertuis, M.-A., Jancu, J.-M. & Katan, C. Electronic model for self-assembled hybrid organic/perovskite semiconductors: Reverse band edge electronic states ordering and spin-orbit coupling. *Phys. Rev. B* **86**, 205301 (2012).

[22] Das, T., Rocquefelte, X. & Jobic, S. Ab initio positioning of the valence and conduction bands of bulk photocatalysts: Proposition of absolute reference energy. *J. Phys. Chem. C* **124**, 19426–19434 (2020). URL https://doi.org/10.1021/acs.jpcc.0c04003. https://doi.org/10.1021/acs.jpcc.0c04003.

[23] Lodeiro, L. *et al.* Methodological issues in first-principle calculations of ch$_3$nh$_3$pbi$_3$ perovskite surfaces: Quantum confinement and thermal motion. *ACS Omega* **5**, 29477–29491 (2020).

[24] Knutson, J. L., , Martin, J. D. & Mitzi, D. B. Tuning the band gap in hybrid tin iodide perovskite semiconductors using structural templating. *Inorg. Chem.* **44**, 4699–4705 (2005).

[25] Even, J., Pedesseau, L., Jancu, J.-M. & Katan, C. Importance of spin-orbit coupling in hybrid organic/inorganic perovskites for photovoltaic applications. *J. Phys. Chem. Lett.* **4**, 2999–3005 (2013).

[26] Traore, B. *et al.* Composite nature of layered hybrid perovskites: Assessment on quantum and dielectric confinements and band alignment. *ACS Nano* **12**, 3321–3332 (2018).

[27] Katan, C., Mercier, N. & Even, J. Quantum and dielectric confinement effects in lower-dimensional hybrid perovskite semiconductors. *Chem. Rev.* **119**, 3140–3192 (2019).